

See discussions, stats, and author profiles for this publication at: <https://www.researchgate.net/publication/309182189>

Electrochemical Modeling of Commercial LiFePO₄ and Graphite Electrodes: Kinetic and Transport Properties and Their Temperature...

Article in Journal of The Electrochemical Society · January 2016

DOI: 10.1149/2.1151613jes

CITATION

1

READS

291

5 authors, including:



Mehrdad Mastali

University of Waterloo

7 PUBLICATIONS 81 CITATIONS

[SEE PROFILE](#)



Mohammad Farkhondeh

University of Waterloo

13 PUBLICATIONS 79 CITATIONS

[SEE PROFILE](#)



Siamak Farhad

University of Akron

33 PUBLICATIONS 363 CITATIONS

[SEE PROFILE](#)



Roydon Fraser

University of Waterloo

131 PUBLICATIONS 1,565 CITATIONS

[SEE PROFILE](#)

Some of the authors of this publication are also working on these related projects:



Electrochemical Battery Thermal Modeling [View project](#)



Cascaded Use and Sustainable Management of Lithium-ion Batteries in Mobility and Stationary Power [View project](#)

All content following this page was uploaded by [Mohammad Farkhondeh](#) on 18 October 2016.

The user has requested enhancement of the downloaded file. All in-text references [underlined in blue](#) are added to the original document and are linked to publications on ResearchGate, letting you access and read them immediately.



Electrochemical Modeling of Commercial LiFePO₄ and Graphite Electrodes: Kinetic and Transport Properties and Their Temperature Dependence

Mehrdad Mastali,^a Mohammad Farkhondeh,^{b,*} Siamak Farhad,^c Roydon A. Fraser,^{a,z} and Michael Fowler^b

^aMechanical and Mechatronic Engineering Department, University of Waterloo, Waterloo ON N2L 3G1, Canada

^bChemical Engineering Department, University of Waterloo, Waterloo, ON N2L 3G1, Canada

^cMechanical Engineering Department, University of Akron, Akron, Ohio 44325, USA

Based on the variable solid-state diffusivity concept, a semi-physical model is developed to simulate the electrochemical performance of commercial LiFePO₄ (LFP) and graphite electrodes. Although the developed model is not accurately describing the phase change process within the active material, it is reliable for engineering applications such as battery management, thermal analysis and management, and aging studies. The developed LFP and graphite models extend previous works by validating the models against galvanostatic charge/discharge experiments conducted at various currents (C/5 to 5C) and temperatures (10°C, 23°C, 35°C, and 45°C). The fidelity of the model is confirmed by the satisfactory fit of the model to the experimental data for two different materials over a wide range of operating conditions. Temperature dependency of transport and kinetic properties of LFP and graphite is analyzed, and yields the activation energies of 86 kJ mol⁻¹ and 20 kJ mol⁻¹ for diffusion of intercalated species in LFP and graphite particles, respectively. The activation energies for charge transfer reaction at the surface of LFP and graphite particles are also found to be 9 kJ mol⁻¹ and 20 kJ mol⁻¹, respectively. The estimated kinetic and transport parameters and their temperature dependencies can be reliably used in thermal, electrochemical, or aging modeling of batteries involving these two materials.

© 2016 The Electrochemical Society. [DOI: 10.1149/2.1151613jes] All rights reserved.

Manuscript submitted February 11, 2016; revised manuscript received September 30, 2016. Published October 15, 2016.

Recent improvements in lithium-ion (Li-ion) battery energy and power densities have made Li-ion batteries good candidates for energy and power sources in electric devices including electric vehicles. A Li-ion battery consists of a high-potential (positive) and a low-potential (negative) porous electrode with an electrolyte-filled separator to mediate between the two electrodes. Many different materials are incorporated as the positive electrode. Among all, LiFePO₄ (LFP), first introduced by Padhi et al.,^{1–3} has received lots of attention due to its durability, stability, low cost, and low environmental impact. The main concerns regarding this material are poor electronic conductivity^{4–6} and low apparent diffusivity,^{7,8} that are improved by coating the particle surfaces with highly conductive (both electronically and ionically) materials, as well as reducing the LFP particle sizes to nano scales. In addition, graphite is the most commonly used negative electrode material in today's commercial Li-ion batteries due to its relatively high theoretical capacity (372 mAh g⁻¹), low equilibrium potential with respect to Li/Li⁺, its higher safety compared to metallic lithium electrode, eco-friendliness, and low cost.^{9,10} Optimizing the design of Li-ion batteries depends on application specifications; therefore, accurate models capable of predicting Li-ion battery behavior under different operating conditions are necessary.

In LFP electrodes, lithiation/delithiation occurs via a two-phase process between Li-poor heterosite and Li-rich triphylite phases.¹ Many different models have been developed to predict the LFP electrode behavior in Li-ion batteries. Most of these models consider both phases coexisting in the same particle wherein the phase boundary gradually moves within the particle upon lithiation/delithiation. Such models include, but are not limited to, core-shell,^{11–14} phase-field,^{15–19} Kolmogorov-Johnson-Mehl-Avrami,^{20–22} and variable solid-state diffusivity (VSSD)^{23–26} models. However, recent high-resolution chemical mapping of LFP electrodes suggests an alternative electrochemical lithiation/delithiation pathway, where particles are filled in a mixed sequential/parallel fashion depending on the overall applied current.^{27–30} 'Many-particle' models are developed upon these observations to qualitatively explain such a collective behavior of electrochemically lithiated/delithiated LFP electrodes. Among all, the mesoscopic many-unit model developed in Ref. 31 is able to predict the electrode behavior under various operating conditions and explain some of its unusual features including the memory effect. The VSSD

model is used in this paper due its simplicity, relatively low computational cost, and accurate prediction of electrode performance. The VSSD model is based on a concentration-dependent chemical diffusivity of guest species within the solid-state host material that mimics a core-shell-like two-phase behavior in LFP particles. It has also been shown that the VSSD model can successfully be incorporated into multi-scale models of full-size Li-ion batteries.^{32,33}

In the graphite particles, the lithiation/delithiation proceeds through multiple stages, each of which can be regarded as a distinct phase.^{34–38} Various models have been reported for graphite electrodes. Most of these models ignore the phase transition process^{39–42} while a few others account for these phase transitions via a modified form of Avrami equation,⁴³ or the VSSD model.^{44–46} It is shown in Ref. 44,45 that, similar to the case of a LFP electrode,²⁴ the VSSD model can capture the moving phase boundary by considering the species chemical potential as the diffusion driving force within the graphite particles. However, the model for graphite has not been validated against experimental data in the referenced works. This paper addresses this deficiency in the literature, and validates the VSSD model for graphite electrode by comparing simulations to galvanostatic charge/discharge voltage data at various charge/discharge rates and electrode temperatures.

A major concern for Li-ion battery models is the accuracy of physico-chemical model parameter estimates and their temperature dependency. In the case of LFP electrodes, few papers report the temperature dependency of the solid-state transport and kinetic properties.^{47–50} In these papers, however, the estimation methods (e.g., electrochemical impedance spectroscopy and resistive-reactant model) rely on simplifying assumptions that may not be consistent with the end-use electrochemical models.^{47–49} Furthermore, Ref. 50 does not provide any information regarding the parameter estimation approach used. Similar inconsistent assumptions, or lack of explanation issues also exists for the temperature dependency of graphite electrode transport and kinetic parameters.^{41,49–53} In addition, in many cases, due to the lack of reliable data, parameters reported for similar but not identical negative electrode materials, such as petroleum coke⁵⁴ and graphitized carbonized cloth,⁵⁵ are used in place of unknown graphite electrode parameters. In some works parameters are assumed for the temperature dependency for transport and kinetic parameters but in no way validated.⁵⁶ Lastly, in Ref. 57 the temperature dependency of graphite kinetic and transport properties is adjusted within a three-dimensional thermal model to fit experimental electrochemical/thermal data. However, the process used in

*Electrochemical Society Student Member.

^zE-mail: rfraser@uwaterloo.ca

Ref. 57 introduces uncertainties in parameter determination since it determines graphite parameters through fitting with a three-dimensional model, which has more degrees of freedom than a half-cell model.

The objective of this work is to expand determination of the transport and kinetic properties for graphite and LFP electrodes at different temperatures. A series of galvanostatic charge/discharge experiments are conducted on electrodes obtained from a commercial graphite/LFP pouch cell for a wide range of C-rates (C/5 to 5C) and temperatures (10°C, 23°C, 35°C, and 45°C). The performance of both electrodes is simulated using the VSSD model that enables the determination of transport and kinetic parameters through experimental data fitting. Having accurate temperature dependency for model parameters is crucial, especially for thermal and aging modeling of large Li-ion batteries and for the design of reliable battery management systems. The reported parameters may be used for temperature conditions relevant to battery operation in applications such as electric or hybrid electric vehicles.

Experimental

The electrode materials used for making graphite and LFP half-cells are from a 20 Ah prismatic lithium-ion battery designed for electric vehicle applications. The prismatic cell is first discharged to 2.0 V at C/10 (constant current) and then held at 2.0 V (constant voltage) until the current response reaches the cutoff value of C/50. Afterwards, the cell is disassembled and cleansed several times using anhydrous dimethyl carbonate (DMC) in an argon-filled glove box (<1 ppm H₂O, <1 ppm O₂). Scanning electron microscopy (SEM) is performed utilizing a Zeiss ULTRA Plus electron microscope on both electrodes to extract the electrode thickness and particle sizes. A P-6 Stylus Profiler (KLA-Tencor, USA) is also used to confirm the electrode thickness. For the electrodes used for electrochemical tests, the coating on one side of the double-sided electrode laminate is carefully removed inside the glove box by means of a cotton-based wipe soaked in N-methyl-2-pyrrolidone (NMP). The graphite and LFP electrodes are then punched using 9.7 and 11.7 mm punchers, respectively. Two half-cells per electrode type (i.e., 2 replicates) are assembled in a CR2032-type coin cell with a 12.7 mm lithium metal disk as the reference/counter electrode and Celgard 2500 polypropylene membrane sheet as the separator between the working and reference/counter electrodes. A 1 mol L⁻¹ solution of LiPF₆ in 1:1 volumetric mixture of ethylene carbonate (EC) and dimethyl carbonate is used as the electrolyte. In addition to the graphite and LFP half-cells, three Li/Li symmetric cells (i.e., 3 replicates) are also assembled inside the glove box to characterize the charge-transfer reaction at the surface lithium metal foil. For the sake of consistency, the same electrolyte, separator, and coin-cell setup are utilized for the symmetric Li/Li cell assembly.

The assembled coin cells are then tested in a Cincinnati Sub-Zero MCB-1.2 (USA) temperature chamber using a Neware CT-3008-5V10 mA-164-U (China) battery cycler. The Li/Li symmetric cells are cycled at 0.16 mA (10 hours in each direction), 0.32 mA (5 hours in each direction), and 0.8 mA (2 hours in each direction) at 23°C, and 35°C after being cycled five times at 0.8 mA (2 hours in each direction) at 23°C (formation cycles). At 10°C, the symmetric cells are cycled at smaller rates of 0.054 mA (30 hours in each direction), 0.08 mA (20 hours in each direction), and 0.16 mA (10 hours in each direction) to assure the electrolyte losses remain negligible. The applied currents are chosen to be close to the values used to cycle the LFP and graphite electrodes assuring similar operating conditions. Before conducting the rate capability experiments, the Li/LFP and Li/graphite cells are cycled five times (formation cycles) at C/2 rate (1C rate is equivalent to 1.696 mA of applied current for the LFP and 1.242 mA for the graphite electrode) between the lower (2.5 V for LFP and 0.005 V for graphite) and upper (4.2 V for LFP and 1.5 V for graphite) cutoff potentials at 23°C. In these cycles, the charge steps are followed by a constant voltage step until the current reaches C/50, while the discharge steps are followed by another constant current step at C/50 until the lower cutoff potential is reached. The rest periods between charge and discharge steps are set to 15 minutes. The rate capability

tests are carried out at 4 different temperatures in the following order: 23°C, 10°C, 35°C and 45°C. The higher temperature tests are conducted last to minimize the influence of side reactions accelerated at high temperatures, which may impact measurements at other temperatures. At 23°C, a series of galvanostatic charge/discharge cycles are conducted at rates C/5, C/2, 1C, 2C, 3C, and 5C, each of which consisting of the following steps: i) charging at a particular rate until the upper cutoff potential is reached, ii) 10-minute rest period, iii) charging at C/50 until the upper cutoff potential is reached again, iv) 1-hour rest period, v) discharging at the same rate as that in step i) until the lower cutoff potential is reached, vi) 10-min rest period, vii) discharging at C/50 until the lower cutoff potential is reached again, and viii) 1-hour rest period. Similar galvanostatic cycling but at one or two rates are conducted at other temperatures in the following sequence: i) C/5 (C/2 and 1C & 2C) charge at 10°C (35°C and 45°C) until the upper cutoff potential is reached, ii) 1-hour rest period, iii) C/5 (C/2 and 1C & 2C) discharge at 10°C (35°C and 45°C) until the lower cutoff potential is reached, iv) 1-hour rest period, v) soaking the cells thermally at 23°C for 3 hours, vi) C/50 discharge at 23°C until the lower cutoff potential is reached again. The latter step is to make sure the electrodes are reached the same fully discharged condition before the next cycle starts. It should also be noted that lower charge/discharge rates are applied at lower temperatures in order to: i) minimize lithium foil overpotential which is a source of error due to the complicated electroplating/stripping process at its surface not accounted for in the model, ii) minimize electrolyte polarization for which accurate estimates of transport properties are not available, iii) minimize potential losses associated with the solid-electrolyte interphase (SEI) layer which is not accounted for in the model, and iv) assure the cell temperature is well controlled at the chamber temperature, i.e., sufficient heat dissipation from the cell. On the other hand, the applied current is increased for cycling at higher temperatures in order to guarantee discernible LFP (graphite) solid-state diffusion as well as charge-transfer reaction limitations. Altogether, these operating conditions assure an acceptable level of signal-to-noise ratio within the constraints posed by the model assumptions.

Mathematical Model

The pseudo-two-dimensional (P2D) model originally introduced by Doyle et al.^{58,59} is incorporated for mathematical modeling of the coin cells assembled in this study. The P2D model combines transport and reaction phenomena occurring at two different levels: particle level and electrode level. The governing equations in the two levels are connected via the electrochemical reactions on the surface of active material particles described by the Butler-Volmer relation. This relation also governs the electrochemical reaction at the surface of the metallic lithium reference/counter electrode. The active particles are considered to be spherical. The active materials are assumed to be non-ideal binary solutions of intercalated species and empty sites wherein the diffusion is driven by the gradient of chemical potential, rather than concentration, of the intercalated species. The effect of non-ideality is manifested in a non-unity concentration-dependent thermodynamic factor, α_k , that scales the binary diffusion coefficient, \mathcal{D} . The thermodynamic factor is extracted from the experimental open-circuit potential of the electrodes. Indeed, the associated phase-change or staging processes in LFP and graphite particles are captured by the resulting variable solid-state diffusivity (VSSD).^{24,60} It should be noted that, the model does not predict phase separation under low currents and open circuit operating conditions. Furthermore, the model incorporates multiple sizes in the particle level to take into account the diversity of the active material particle sizes. At the electrode level, the charge balances across the solid (active material and conductive matrix) and liquid (electrolyte filling the pores) phases as well as lithium ion mass balance in the liquid phase are solved. The governing equations together with corresponding boundary conditions are represented in Table I. For the variable definitions, refer to the nomenclature or Refs. 25,61. The half-cell operating voltage is

Table I. The Governing equations and corresponding boundary conditions of the pseudo-two-dimensional model.³³

Particle-level governing equations	
Cathode active materials	Boundary conditions
$\frac{\partial c_{s,k}}{\partial t} = \frac{1}{r_k^2} \frac{\partial}{\partial r_k} (r_k^2 \alpha_k D \frac{\partial c_{s,k}}{\partial r_k}) \alpha_k = -\frac{F}{RT} y_k (1 - y_k) \frac{\partial U_k}{\partial y_k},$ $y_k = c_{s,k}/c_s^{max} i_{n,k} = i_k^0 [\exp(\frac{(1-\beta)F}{RT} \eta_k) - \exp(\frac{-\beta F}{RT} \eta_k)] \eta_k = \phi_s - \phi_e - U_k,$ $i_k^0 = F k_c^0 c_e^{1-\beta} c_s^{max} (1 - y_k)^{1-\beta} y_k^\beta$	$\frac{\partial c_{s,k}}{\partial r_k} _{r_k=0} = 0 \alpha_k D \frac{\partial c_{s,k}}{\partial r_k} _{r_k=R_{p,k}} = \frac{i_{n,k}}{F} c_{s,k} _{t=0} = c_{s,k}^0$
Electrode-level governing equations	
Cathode	Boundary conditions
$\nabla \cdot (\sigma_c^{eff} \nabla \phi_s) = \sum a_k i_{n,k}$ $\sigma_c^{eff} = \sigma_c (1 - \varepsilon_c)^\gamma \nabla \cdot (-\kappa_c^{eff} \nabla \phi_e) + \nabla \cdot (\kappa_{D,c}^{eff} \nabla \ln c_e) = \sum a_k i_{n,k} \kappa_c^{eff} = \kappa_c \varepsilon_c^\gamma,$ $\kappa_{D,c}^{eff} = \frac{2RT\kappa_c^{eff}}{F} (1 - t_+^0) (1 + \frac{d \ln f_{\pm}}{d \ln c_e}) \frac{\partial (\varepsilon_c c_e)}{\partial t} =$ $\nabla \cdot (D_{e,c}^{eff} \nabla c_e) + \frac{1-t_+^0}{F} \sum a_k i_{n,k} D_{e,c}^{eff} = D_e \varepsilon_c^\gamma$	$\sigma_c^{eff} \nabla \phi_s _{x=L_s} = 0$ $\sigma_c^{eff} \nabla \phi_s _{x=L} = I_{app} \kappa_c^{eff} \nabla \phi_e _{x=L} = 0 \text{ continuity at } x = L_s$ $D_{e,c}^{eff} \nabla c_e _{x=L} = 0 \text{ continuity at } x = L_s \quad c_e _{t=0} = c_e^0.$
Separator	Boundary conditions
$\nabla \cdot (-\kappa_s^{eff} \nabla \phi_e) + \nabla \cdot (\kappa_{D,s}^{eff} \nabla \ln c_e) = 0 \quad \kappa_s^{eff} = \kappa_s \varepsilon_s^\gamma,$ $\kappa_{D,s}^{eff} = \frac{2RT\kappa_s^{eff}}{F} (1 - t_+^0) (1 + \frac{d \ln f_{\pm}}{d \ln c_e}) \frac{\partial (\varepsilon_s c_e)}{\partial t} = \nabla \cdot (D_{e,s}^{eff} \nabla c_e) \quad D_{e,s}^{eff} = D_e \varepsilon_s^\gamma$	$\phi_e _{x=0} = 0 \text{ continuity at } x = L_s \quad D_{e,s}^{eff} \frac{\partial c_e}{\partial x} _{x=0} = -\frac{I_{app}(1-t_+^0)}{F}$ $\text{continuity at } x = L_s \quad c_e _{t=0} = c_e^0$
Lithium foil electrode	
$I_{app} = F \varepsilon_s k_{Li}^0 c_e^{1-\beta_{Li}} [\exp(\frac{(1-\beta_{Li})F}{RT} (\phi_{Li} - \phi_e)) - \exp(\frac{-\beta_{Li}F}{RT} (\phi_{Li} - \phi_e))]$	

then calculated from Equation 1:

$$V_{cell} = \phi_s |_{x=L} - \phi_{Li} \quad [1]$$

The system of nonlinear algebraic partial differential equations in Table I is solved by finite element methods using the COMSOL Multiphysics software.⁶² Both the separator and electrode regions are discretized into 10 equal elements across their thickness. Since azimuthal and zenithal variations inside the active particles are neglected, the LFP and graphite particles are solved on a grid consisting of 20 elements along the radial direction. This grid becomes finer as approaching the particle surfaces and the ratio between smallest element at the surface to the largest element around the center is 0.2.

Results and Discussion

The experiment and simulation results are presented in this section. Three subsections dedicated to Li foil, LFP electrode, and graphite electrode are included here. The main purpose is to use mathematical models for the Li/LFP and Li/graphite half-cells to estimate the kinetic and transport properties of LFP and graphite and their temperature dependencies. To this end, the model is fitted to the experimental data, as is described later in this section. Active particle-size distributions (PSD) for the LFP and graphite electrodes are estimated by examining ~270 and ~330 particles counted across the SEM images, respectively. It is not required to incorporate the complete size distribution, rather, based on the operating voltage curves of the half-cells, a minimum number of particle bins representing the entire PSD is used without compensating for accuracy.²⁴ The minimum number of particle bins is determined by the overall error between simulation results and experimental data being 1% or less.

Li foil kinetics temperature dependency.—Prior to the determination of the temperature dependency of the LFP and graphite lithiation/delithiation dynamics, it is required to determine the temperature dependency of charge-transfer kinetics at the surface of the metallic lithium reference/counter electrode in order to separate associated potential losses. As explained in Experimental section, three different currents in each charge or discharge direction (total of six) are applied to three Li/Li cell replicates maintained at three different temperatures and the voltage response of the cell to each applied current is recorded. The recorded potential differences are averaged to yield single values for each of the six measurements. It is assumed that both lithium electrodes in the symmetric cells contribute the same to the output potential difference; hence, to obtain the surface overpotential of each electrode, the averaged potential difference is di-

vided by two. The Butler-Volmer relation is fitted to the experimental data using the Matlab's nonlinear least-square curve fitting routine 'lsqcurvefit'.⁶³ The charge transfer coefficient is set to be 0.5⁶⁴ and the gradient of electrolyte concentration and potential across the separator ($L_s = 25 \times 10^{-6}$ m) is neglected under the experimental conditions. This is a valid assumption since the diffusion time constant of the electrolyte in the separator ($\tau_D = L_s^2/D_e^{eff}$) is ~5 s at 23°C which is negligible compared to the operating time of the Li/Li cells. In addition, the potential loss due to the ionic migration across the separator is calculated to be less than 0.45 mV which is, again, negligible compared to the measured potential difference across the symmetric cells. Figure 1 shows both the averaged experimental data points and the fitted curves for all three temperatures. As seen, the fitted curves are almost linear in the current density range of consideration in this work. If the exponential function in the Butler-Volmer relation is estimated by the first term of its Taylor expansion about the zero lithium foil potential, the slope of fitted lines is $\frac{RT}{F^2 \varepsilon_s k_{Li}^0 c_e^{1-\beta_{Li}}}$. The estimated rate constants of electrochemical reaction at lithium foil are given in Table II, which are well in the range of reported values in the literatures.^{58,65,66}

Since the rate constant of electrochemical reaction obeys Arrhenius behavior, the following relation explains its temperature

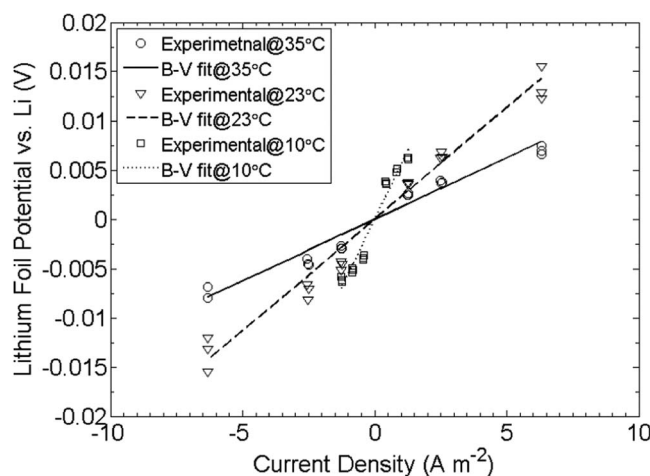


Figure 1. Surface overpotential of metallic Li electrode measured as a function of the applied current density at 10°C, 23°C, and 35°C (symbols) and the curve fit using the Butler-Volmer relation (lines).

Table II. The electrochemical reaction rate constants at the lithium foil for different temperatures.

Temperature (°C)	Rate constant, k_{Li}^0 , (mol/[m ² s(mol/m ³) ^{0.5}])
10	2.62×10^{-6}
23	6.64×10^{-6}
35	1.21×10^{-5}

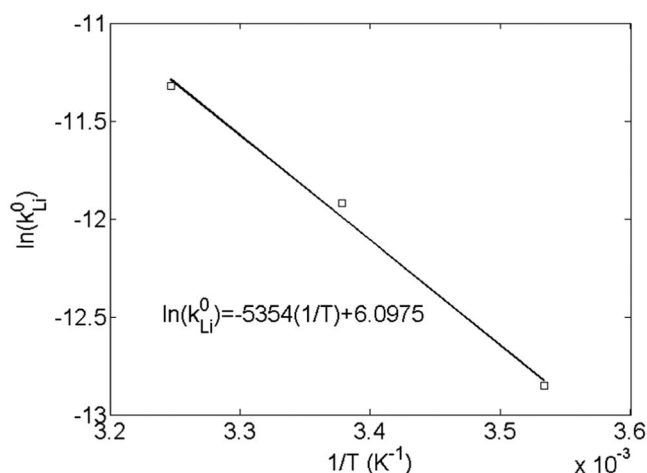
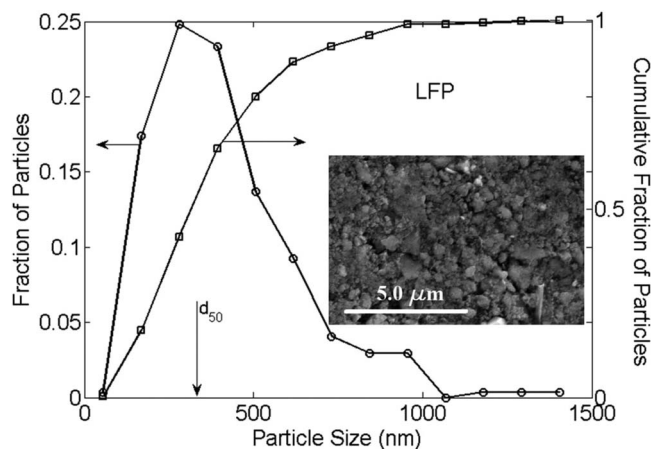
dependency:^{51,54,67}

$$\ln(k_{Li}^0) = \frac{-E_{k_{Li}}^a}{R} \left(\frac{1}{T} \right) + C_1 \quad [2]$$

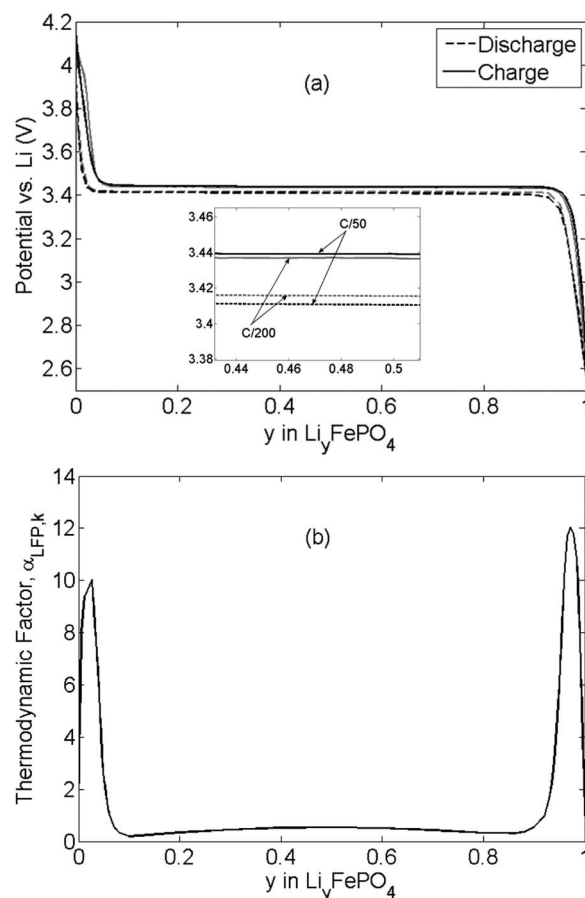
where $E_{k_{Li}}^a$ is the activation energy of charge-transfer reaction at the lithium electrode, R is the universal gas constant, T is the temperature, and C_1 is a constant with regard to temperature. The activation energy and the constant are then determined by least square curve fitting to the rate constants obtained for the three temperatures. Figure 2 depicts the logarithm of the rate constant of the charge-transfer reaction at the metallic lithium electrode fitted by the Arrhenius equation. Therefore, the determined activation energy of charge-transfer reaction at the lithium electrode and the constant of Equation 2 are 45 kJ mol⁻¹ and 6.0975, respectively.

Li_yFePO₄ electrode.—In this section, a Li/LFP half-cell is modeled. First, the required parameters are obtained mostly from non-electrochemical measurements and then the rest of the parameters are estimated by fitting the model to the experimental galvanostatic charge/discharge data. In the inset of Figure 3, an SEM image taken of the LFP electrode is given. Although the active particles are partially agglomerated and have various shapes, it is assumed that they are spherical and grouped into 13 different bins. The resulting PSD is shown in Figure 3 where particle sizes range from ~0.05 μm to ~1.4 μm with the median diameter (d_{50}) of ~320 nm.

Separate LFP equilibrium potentials are considered for charge and discharge simulations of the Li/LFP half-cell.²⁴ The charge/discharge equilibrium potential of the LFP electrode is obtained by slowly charging/discharging the LFP electrode at a C/50 rate and at 23°C. The lithium foil is taken to be the reference electrode; hence, given a slow enough applied current, the recorded cell voltage approximates the LFP electrode equilibrium potential. As seen in Figure 4a, the equilibrium potential measured during C/50 charge is almost ~0.03 V higher than the equilibrium potential measured during C/50 discharge. This potential gap is of thermodynamic nature for the most part and approaches the so-called “quasi-static” potential hysteresis⁶⁸ when the

**Figure 2.** The logarithm of the electrochemical reaction rate constant at metallic lithium electrode, $\ln(k_{Li}^0)$, as a function of the inverse of temperature.**Figure 3.** Particle size distribution of LFP electrode from an analysis of SEM image shown in the inset.

applied current is reduced; it is not explained by the VSSD model^{24,31} and is, therefore, excluded from the analysis by taking two separate equilibrium potentials one on charge and one on discharge as mentioned above. Figure 4a also shows the equilibrium potential of the LFP electrode obtained by charging/discharging the LFP electrode at C/200. It is shown that a 4-fold decrease in the operating rate from C/50 to C/200 does not lead to a significant drop in electrode polarization. As a result, it is safe to use C/50 charge/discharge data to approximate the electrode equilibrium potential. The temperature

**Figure 4.** (a) The equilibrium potentials, $U_{LFP,k}$, and (b) the thermodynamic factor, $\alpha_{LFP,k}$, used for discharge and charge simulations of the LFP electrode.

dependency of the LFP equilibrium potential is directly proportional to the entropy change of the electrode due to changes in the extent of lithiation/delithiation ($(\frac{\partial U_{LFP}}{\partial T})_{P,y} = \frac{\Delta S(y)}{nF}$). This correlation can be approximated by Taylor's expansion as follows:

$$U_{LFP}(y, T) = U_{LFP}(y, T_R) + \frac{\partial U_{LFP}}{\partial T}|_{y,T_R} (T - T_R) \quad [3]$$

where T_R is the reference temperature. Dodd et al.^{69,70} reported entropy change, $\Delta S(y)$, as a function of lithium concentration. They charged or discharged the Li/LFP half-cell at C/20 rate in 5% SOC steps. At each step, the half-cell was cooled down using a Peltier plate to five temperatures between the room temperature and 12°C and the equilibrium potential was recorded for each temperature. The variation of LFP electrode equilibrium potential with respect to temperature was then used to determine the entropy change at the specified SOCs. The reported entropy change is, however, very small for all lithium concentrations and therefore ignored in this study. Although the LFP base material is the same, the electrode studied by Dodd may differ in active particle sizes, and impurities and defects, to that studied in this paper; it is nonetheless assumed that these possible differences are negligible. It should be noted that other papers also reported similar values for entropy change as a function of lithium content of LFP electrode.^{71,72}

The phase-change process within the electrode particles is approximated by considering a non-unity thermodynamic factor, $\alpha_{LFP,k}$, also known as the activity-correction factor,²⁴ in the diffusion equation. Experimentally, the thermodynamic factor is found to differ for charging than for discharging (i.e., due to difference in equilibrium potentials considered), however physically it should be the same. Therefore, the best estimate used for the thermodynamic factor in this work is the average of the thermodynamic factors calculated from C/50 galvanostatic charge and discharge data (i.e., assumed equilibrium potentials). The thermodynamic factors are determined by the numerical differentiation of the equilibrium potentials following Equation 4:^{24,60}

$$\alpha_{LFP,k} = -\frac{F}{RT} y_{LFP,k} (1 - y_{LFP,k}) \frac{\partial U_{LFP,k}}{\partial y_{LFP,k}} \quad [4]$$

where F is the Faraday's constant, y_{LFP} is the lithium mole fraction in the LFP particles, U_{LFP} is the charge/discharge equilibrium potential for LFP, and the subscript k represents the k^{th} bin of particles. The result is shown in Figure 4b where the maxima at both ends of the diagram correspond to the single lithium poor and lithium rich phases, or high and low SOC regions, respectively. Very small thermodynamic factor values in the intermediate composition range, which is between the lithium poor and lithium rich regions, results in low Fickian diffusivities and a sharp concentration profile that resembles a moving phase boundary.²⁴ It should be noted that, although a two-phase lithiation/delithiation mechanism theoretically requires the equilibrium potential as a function of composition to appear as a perfect plateau in the mid stoichiometry range, the actual electrode potential is never perfectly flat⁷³ regardless of the measurement conditions. This gives rise to a very small but non-zero thermodynamic factor as a means for approximating the presumed phase-boundary movement across LFP particles.

The electrolyte transport and thermodynamic properties for LiPF₆ in PC/EC/DMC solution as a function of temperature and concentration are adopted from Ref. 74. Although the electrolyte of Ref. 74 differs from the one used in the coin cells studied in this paper, it is assumed that both electrolytes have similar properties as a function of temperature given the additional PC in Ref. 74 is a small fraction, 10 percent, of the total electrolyte. This assumption is required due to the lack of measurements of transport and thermodynamic properties in the literature for LiPF₆ in EC/DMC. All the properties from Ref. 74 are valid for temperatures between -10°C and 60°C and for LiPF₆ concentrations ranging from 0.4 mol L⁻¹ to 3.3 mol L⁻¹. The ionic conductivity of the electrolyte, κ , in mS cm⁻¹ is expressed as

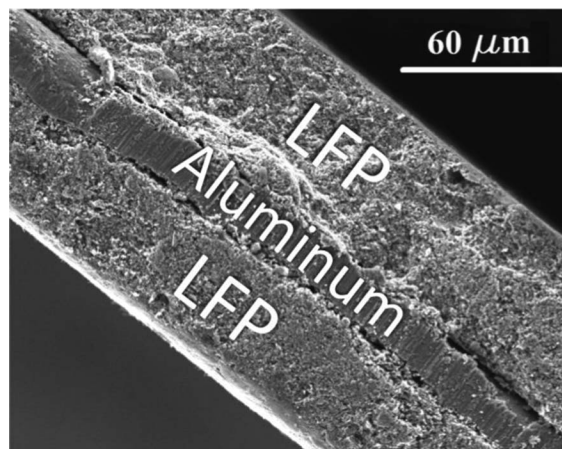


Figure 5. The SEM image of the cross-section of a double-sided LFP electrode.

follows:

$$\begin{aligned} \kappa(c_e, T) = & c_e(-10.5 + 0.0740T - 6.96 \times 10^{-5}T^2 + 0.668c_e \\ & - 0.0178c_eT + 2.80 \times 10^{-5}c_eT^2 + 0.494c_e^2 \\ & - 8.86 \times 10^{-4}c_e^2T)^2 \end{aligned} \quad [5]$$

where c_e is the electrolyte concentration in mol L⁻¹, and T is the temperature in K. In addition, the diffusion coefficient of the electrolyte, D_e , in cm² s⁻¹ is as follows:

$$\log_{10} D_e(c_e, T) = -4.43 - \frac{54}{T - (229 + 5.0c_e)} - 0.22c_e \quad [6]$$

Finally, the electrolyte thermodynamic factor is given as follows:

$$\begin{aligned} & \left(1 + \frac{d \ln f_{\pm}}{d \ln c_e}\right) \\ & = \frac{1}{1 - t_+^0} \left[0.601 - 0.24c_e^{\frac{1}{2}} + 0.982(1 - 0.0052(T - T_0))c_e^{\frac{3}{2}}\right] \end{aligned} \quad [7]$$

where T_0 is the reference temperature with the value of 294 K, and the t_+^0 is the lithium ion transference number whose value is 0.38.⁷⁴ It should be noted that there is a discrepancy between the assumptions adapted here and those considered in Ref. 74 for electrolyte parameter estimation. The above estimates of the transport and thermodynamic properties are measured assuming non-zero convection in the electrolyte whereas convection is neglected in the model developed here. However, this inconsistency, in addition to the difference in the electrolyte composition, is expected not to introduce significant errors in the model predictions and is, therefore, ignored.

The thickness of the LFP electrode coating was measured to be 59 μm using the profilometer after carefully stripping away a portion of the electrode coating on one side of the double-sided LFP electrode (see Figure 5). The profilometer scanned the surface of the LFP electrode, and then moved into the region of only the aluminum current collector thus providing a measure of the thickness of the missing electrode coating. An SEM image as shown in Figure 5 did not yield an accurate measure for the thickness of the electrode coating as SEM sample cross-sections (factory-cut) were likely distorted due to the mechanical pressure applied locally by the cutter. This distortion can be seen in Figure 5 as the total thickness in the SEM is ~122 μm while that measured away from the electrode edge (using a micrometer) is ~137 μm. In contrast, the thickness of the aluminum can be measured on the SEM image at 19 μm as the cutter does not noticeably compress or distort the aluminum.

The capacity of the LFP electrode is assumed to be equal to the total charge throughput measured at the end of C/50 galvanostatic

discharge at the cutoff voltage of 2.5 V. From the experimental data, a capacity of 1.696 mAh is obtained for the LFP electrode. Given the puncher size (11.7 mm for LFP), the area of the LFP electrode is also known. Using the LFP thickness determined above, and the capacity and area, as well as the theoretical capacity and density of LFP, which are 170 mAh gr^{-1} and 3.6 gr cm^{-3} ,³ respectively, the active material volume fraction of the LFP electrode is calculated to be ~ 0.437 . If a typical 0.1 volume fraction is considered for the binder and conductive materials in the LFP electrode,⁷⁵ the porosity of the LFP electrode is then estimated to be ~ 0.463 . Based on the available data from the manufacturer,⁷⁶ the thickness and porosity of the separator are 25 μm and 0.55, respectively.

Aside from the electrochemical reaction rate constant, k_{LFP}^0 , and solid-state binary diffusion coefficient, D_{LFP} , and the parameters determined in the previous two paragraphs, the other parameters are considered fix and depend on electrode morphology (the Bruggeman exponent, γ), electrolyte composition (initial electrolyte concentration, c_e^0), known material properties (maximum lithium concentration in LFP, c_{LFP}^{max}), and assumed kinetics of anodic/cathodic reactions (charge transfer coefficient, β). As mentioned in Experimental section, the initial electrolyte concentration is 1 mol L^{-1} . The maximum lithium concentration is assumed to be constant at 22,806 mol m^{-3} since the LFP density is considered to be independent of lithium concentration.¹⁴ The Bruggeman exponent and the charge transfer coefficient are set to 1.5 and 0.5, respectively.^{25,77,78}

The electrochemical reaction rate constant and solid-state binary diffusion coefficient are estimated by fitting the model to the experimental galvanostatic charge/discharge data. Given a single particle size obtained from the SEM image analysis (i.e., d_{50}), this provides two degrees of freedom for minimizing the difference between model and experiment. The rate constant primarily affects the match to the experiment in the onset and plateau regions of the operating voltage curves, and the diffusion coefficient primarily affects the match to experiment in the end-capacity region of the operating voltage curves. Through manual iteration the difference between the experiment and simulation results was minimized. The rate constant using the two degree-of-freedom model is determined to be of $8.8 \times 10^{-12} \text{ mol}/[\text{m}^2\text{s}(\text{mol}/\text{m}^3)^{1.5}]$ at 23°C which is in agreement with the reported values in the literature.^{24,25,73} The rate constant is considered to be independent of applied current, consistent with,^{24,25,73} but contrary to.⁶⁶ The end-capacity region of the experimental data is used to determine the binary diffusion coefficient; however, it generates a poor fit to the experimental data as long as only one particle size is considered as similarly observed by Farkhondeh and Delacourt.²⁴ In other words, the effect of the non-uniform particle size distribution, rather than only the median particle size, should be taken into account^{14,24,26} leading to an increase in the number of degrees of freedom.

It has been shown that inclusion of the actual PSD obtained from the SEM image analysis (Figure 3) in the model does not yield a good fit to the end-capacity region of the experimental galvanostatic charge/discharge data regardless of the number of bins.²⁴ Consequently, trial and error iteration was used to determine the number of particle bins, their sizes, and their volume fraction in order to obtain a reasonably good fit. As more particle bins are added to the model, the end-capacity fit to experiment continually improves as shown in Ref. 25, however, this accuracy comes in the cost of higher computational effort. Therefore, in order to keep the computational effort reasonable, the number of particles added to improve the fit should be as small as possible while still yielding a good model-to-experiment fit. Eventually four particle bins were selected as providing a good compromise between accuracy and computational cost. This fitting process involved an increase in the corresponding degrees of freedom from one, for the binary diffusion coefficient, to seven when both the size and volume fractions of the three additional particle bins are added. Table III lists d_{50} and the adjusted bin sizes together with their volume fractions. The adjusted PSD is well within the range of the PSD obtained experimentally. Along with the adjusted PSD, the resulting fit of the model to the experimental voltage data, seen in Figure 6, yields the solid-state binary diffusion coefficient of Li inside LFP particles.

Table III. Particle size distribution of the LFP electrode obtained by fitting the simulation results to the experimental galvanostatic discharge data at all C-rates ranging from C/5 to 5C at 23°C.

Particle group	Particle size, $2R_{LFP,k}$ (nm)	Volume fraction, $\epsilon_k/\epsilon_{t,LFP}$
1	160 ^f	0.4 ^f
2	320 ^m	0.41 ^f
3	680 ^f	0.12 ^f
4	1500 ^f	0.07 ^c

(f: fitted, m: measured (d_{50}), and c: calculated using $1 - \sum_{k=1}^3 \epsilon_k/\epsilon_{t,LFP}$).

The asymmetry observed in Figure 6 between the charge and discharge end-capacities for different C-rates is consistent with the observations of Srinivasan and Newman.⁷⁹ This phenomenon is commonly attributed to the different transport properties in the lithium-poor and lithium-rich phases.^{66,79–81} Safari and Delacourt^{49,66} considered this effect in their resistive-reactant model by assuming a larger diffusion coefficient for the lithium-poor phase, while Farkhondeh and Delacourt²⁴ adjusted the thermodynamic factor in their variable diffusivity model to capture this behavior. In this paper, however, in an effort to minimize the additional degrees of freedom needed to capture the asymmetry between charge and discharge end-capacities, the approach of Farkhondeh and Delacourt²⁴ is not used. If the approach of Farkhondeh and Delacourt²⁴ was to be used it would require adjusting the ‘shape’ of the thermodynamic factor at each temperature and making this parameter a function of temperature as well as lithium concentration. Instead, this paper utilizes two different temperature dependent binary diffusion coefficients for charge and discharge simulations as discussed in more detail in LiFePO₄ properties

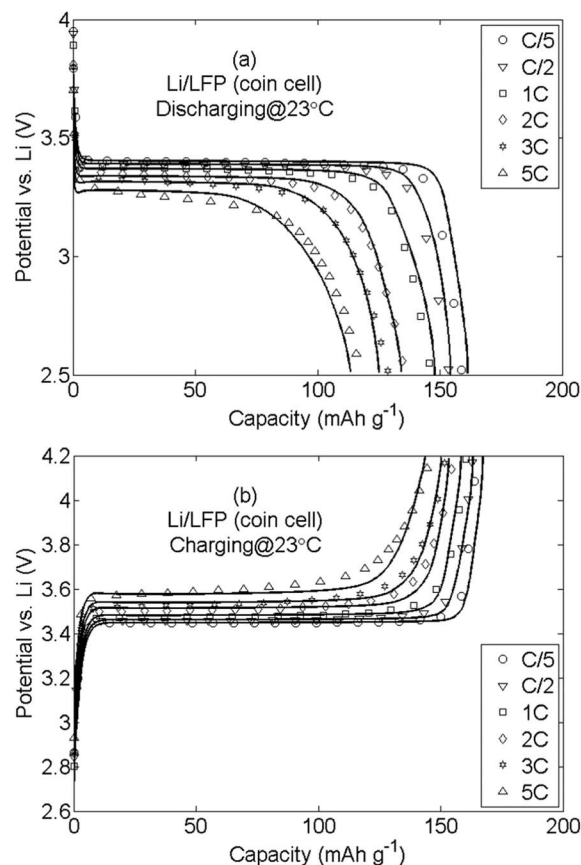


Figure 6. Comparison between the experimental data (symbols) and simulations (solid lines) of the Li/LFP half-cell for (a) galvanostatic discharge and (b) galvanostatic charge rates ranging from C/5 to 5C at 23°C.

Table IV. List of the model parameters used for Li/LFP half-cell simulations at 23°C.

Parameter	Symbol	Value
LFP charge-transfer coefficient	β_{LFP}	0.5 ^a
Li foil charge-transfer coefficient	β_{Li}	0.5 ^a
Bruggeman exponent	γ	1.5 ^a
Initial salt concentration in the electrolyte (mol m ⁻³)	c_e^0	1000 ^s
Maximum Li concentration in the LFP particles (mol m ⁻³)	c_{LFP}^{max}	22,806 ^{fa}
Discharge-fitted binary diffusion coefficient in LFP (m ² s ⁻¹)	\mathcal{D}_{LFP}^d	5.5×10^{-18f}
Charge-fitted binary diffusion coefficient in LFP (m ² s ⁻¹)	\mathcal{D}_{LFP}^c	3.0×10^{-17f}
Porosity of the separator	ε_s	0.55 ^{ce}
Porosity of the LFP electrode	ε_{LFP}	0.463 ^c
Total active material volume fraction of the LFP electrode	$\varepsilon_{t,LFP}$	0.437 ^c
Electrochemical reaction rate constant of LFP (mol/[m ² s(mol/m ³) ^{1.5}])	k_{LFP}^0	8.8×10^{-12f}
Separator thickness (m)	L_s	25×10^{-6ce}
LFP electrode thickness (m)	L_{LFP}	59×10^{-6m}
Effective electronic conductivity of the LFP electrode (S m ⁻¹)	σ_{LFP}^{eff}	6.75 ^e
Li ⁺ transference number	t_+^0	0.38 ^v
Geometric area of the LFP electrode (m ²)	A_{LFP}	1.057×10^{-4m}
Lower cutoff potential of the LFP electrode (V)	$V_{cut,LFP}^{min}$	2.5
Upper cutoff potential of the LFP electrode (V)	$V_{cut,LFP}^{max}$	4.2

(a: assumed, s: set, f: fitted, c: calculated, m: measured, fa: Farkhondeh et al.,²⁵ ce: Celgard,⁷⁶ e: Ender et al.,⁹¹ v: Valoen and Rimeres⁷⁴).

temperature dependency section. The obtained value for the discharge- and charge-fitted binary diffusion coefficients at 23°C, for instance, are $5.5 \times 10^{-18} \text{ m}^2 \text{ s}^{-1}$ and $3.0 \times 10^{-17} \text{ m}^2 \text{ s}^{-1}$, respectively. These values are well within the range reported in the literature.^{24,48,66,82,83} Discharge- and charge-fitted binary coefficients at other temperatures are provided in Table V in LiFePO₄ properties temperature dependency section as part of the LiFePO₄ temperature effects results and discussion.

It has been shown in Ref. 84 that the Butler-Volmer relation is a valid model as compared to Marcus theory for charge-transfer reaction at the surface of LFP if the reaction overpotential is smaller than ~100 mV. Our computation results suggest that the surface overpotential always remains less than 100 mV during discharge and only slightly exceeds this threshold at the very end of high-rate charge for the larger particles. Therefore, the Butler-Volmer relation is considered to be valid for the operating conditions of interest in this work. Finally, all the measured, calculated, and adjusted model parameters for Li/LFP half-cell simulations are summarized in Table III and Table IV. The results of the Li/LFP half-cell simulations together with the experimental data for all galvanostatic discharge and charge rates ranging from C/5 to 5C at 23°C are presented in Figure 6. Good agreement between the experimental data and simulation results is observed in all charge and discharge rates.

LiFePO₄ properties temperature dependency.—Both transport and kinetic properties of LFP are functions of temperature. Generally, an Arrhenius relation is considered to describe temperature dependency of rate constants and solid-state diffusion coefficients.^{51,54,67} Therefore, for LFP one can write,

$$\ln(k_{LFP}^0) = \frac{-E_{k_{LFP}^0}^a}{R} \left(\frac{1}{T} \right) + C_2 \quad [8]$$

$$\ln(\mathcal{D}_{LFP}) = \frac{-E_{\mathcal{D}_{LFP}}^a}{R} \left(\frac{1}{T} \right) + C_3 \quad [9]$$

where $E_{k_{LFP}^0}^a$ is the activation energy of the charge-transfer reaction at the surface of LFP particles, $E_{\mathcal{D}_{LFP}}^a$ is the activation energy of the solid-state diffusion of Li⁺ within LFP, and C_2 and C_3 are constants with regard to temperature. The activation energies, and C_2 and C_3 , in Equations 8 and 9 are evaluated by fitting the mathematical model

to the experimental galvanostatic charge and discharge data at the four temperatures of 10°C, 23°C, 35°C, and 45°C. Recall from Li foil kinetics temperature dependency section, the model also includes temperature dependencies for the electrolyte parameters and for the kinetic parameters of the metallic lithium reference/counter electrode. The results for discharge and charge rates ranging from C/5 to 5C at 23°C are illustrated in Figure 6. The results for 10°C, 35°C, and 45°C are presented next.

As explained in Experimental section, the experiments for 10°C and 35°C were conducted at C/5 and C/2 charge and discharge rates, respectively, and at 1C and 2C rates for 45°C. Again, the electrochemical reaction rate constant for LFP is used to fit the onset and plateau regions of the experimental data while the binary diffusion coefficient is varied to capture the end-capacities. Other model parameters including the adjusted PSD remained unchanged. It should be noted that at 10°C, 35°C, and 45°C, the Li/LFP half-cell is charged first at a given rate and then discharged at the same C-rate. As a result, the electrode is not fully delithiated at the beginning of the discharge processes. For example, when the battery is discharged at 1C it would have been charged at 1C, however, to fully delithiate the electrode the C-rate would need to be reduced as full capacity is approached. Therefore, the initial lithium content of the LFP electrode is adjusted in the model to fit the operating voltage of the cell at the beginning of discharge. In contrast the Li/LFP half-cell is fully discharged at the beginning of the charge processes, according to the experimental protocol followed. The resulting best fits to the galvanostatic discharge and charge data at temperatures of 10°C, 35°C, and 45°C are shown in Figure 7. Good agreement between the experimental data and simulation results is achieved in all charge and discharge rates and temperatures. The estimated electrochemical reaction rate constants and binary diffusion coefficients for LFP are given in Table V.

Linear least square fitting Equations 8 and 9 to the parameter values in Table V yields the corresponding activation energies and constants as given in Table VI.

Figure 8 and Figure 9 show the curve fits used to arrive at the activation energies and constants in Table VI. Note the shift in $\ln \mathcal{D}_{LFP}$ as a function of $1/T$ in Figure 9 between the values estimated on charge and those on discharge. It turns out that, the temperature dependencies of charge- and discharge-fitted binary diffusion coefficients are the same and the estimated activation energies are identical. In general, temperature increase favors the kinetic and transport properties of the active material and improves electrochemical performance of the

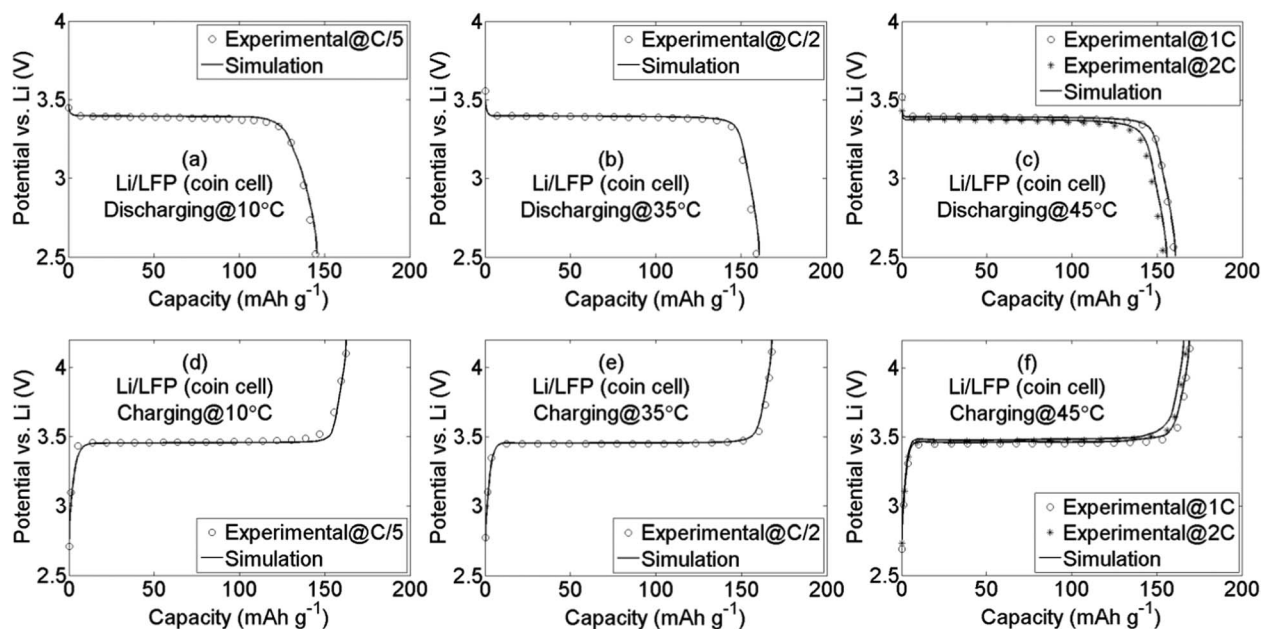


Figure 7. Fitting the experimental galvanostatic discharge and charge data with the mathematical model for (a) discharge at 10°C, (b) discharge at 35°C, (c) discharge at 45°C, (d) charge at 10°C, (e) charge at 35°C, and (f) charge at 45°C for a Li/LFP half-cell.

electrode. However, increasing the temperature has drawbacks such as an accelerated degradation or an increased risk of thermal runaway fires. Note that the activation energy for the electrochemical reaction is approximately an order of magnitude smaller than that for the solid-state diffusion. This means that solid-state diffusion within the LFP particles is thermally activated more pronouncedly as compared to the charge-transfer reaction at the surface of the LFP particles. This leads to a much stronger improvement in solid-state diffusion upon an increase in temperature compared to the charge-transfer reaction.

Having demonstrated the ability of the presented electrochemical model to capture the temperature dependence of the operating voltage for a Li/LFP half-cell, it is useful to summarize how this model compares to other relevant models presented in the literature that also capture the operating voltage well. The result of this comparison is given in Table VII which shows the differences of the model compared to other similar models when used for the galvanostatic charge/discharge operating condition.

Graphite electrode.—This section presents the simulation results of a Li/graphite half-cell. Similar to Li_xFePO_4 electrode section, the parameters of the model are primarily obtained from separate non-electrochemical measurements and the rest of parameters including the electrochemical reaction rate constant and binary diffusion coefficient are obtained by fitting the model to experimental galvanostatic

discharge and charge data. The temperature dependency of kinetic and transport properties of graphite is also discussed. In the inset of Figure 10, an SEM image of the graphite electrode is shown. In contrast to the LFP electrode, which contains mostly spherical-shaped particles, the graphite has a distinctly flaky morphology. For the sake of modeling, however, the graphite flakes are modeled as spherical particles. Due to the broad range of particle sizes observed in the SEM image, the graphite particles are categorized into 25 bins to give a good representation of the shape of the particle size distribution. Counting the particles/flakes in each bin gives the PSD of the graphite electrode as observed in Figure 10. The graphite particle diameters vary from $\sim 0.25 \mu\text{m}$ to $\sim 13.2 \mu\text{m}$ with the median diameter (d_{50}) of $\sim 2.9 \mu\text{m}$.

Separate graphite equilibrium potentials are considered for Li/graphite half-cell discharge and charge simulations. Similar to the LFP electrode, the equilibrium potentials are obtained by discharging/charging the Li/graphite half-cell at a very slow operating rate of C/50 and at 23°C. The lithium electrode is taken as the reference electrode, and thus the output voltage approximates the equilibrium potential of the graphite as a function of lithium concentration in graphite. Due to the lithium intercalation/deintercalation in the discharge/charge process, the entropy of the graphite electrode changes giving rise to a temperature dependent equilibrium potential. Reynier et al.^{85,86} estimated this entropy change by measuring the equilibrium potential of an electrically-insulated Li/graphite half-cell placed in a

Table V. The estimated kinetic and transport parameters for LFP at different temperatures.

Temperature (°C)	Operating rate	Electrochemical reaction rate constant, k_{LFP}^0 , (mol/[m ² s(mol/m ³) ^{1.5}])	Discharge-fitted binary diffusion coefficient, \mathcal{D}_{LFP}^d , (m ² s ⁻¹)	Charge-fitted binary diffusion coefficient, \mathcal{D}_{LFP}^c , (m ² s ⁻¹)
10	C/5	7.5×10^{-12}	9.0×10^{-19}	7.3×10^{-18}
23	C/5 to 5C	8.8×10^{-12}	5.5×10^{-18}	3.0×10^{-17}
35	C/2	1.0×10^{-11}	1.9×10^{-17}	1.3×10^{-16}
45	1C & 2C	1.15×10^{-11}	5.1×10^{-17}	4.0×10^{-16}

Table VI. The activation energies and Equations 8 and 9 constants used to describe the temperature dependency of the kinetic and transport properties of LFP.

Parameter	Electrochemical reaction rate constant	Discharge-fitted binary diffusion coefficient	Charge-fitted binary diffusion coefficient
Activation energy (J mol ⁻¹)	9×10^3	8.6×10^4	8.6×10^4
Constants	$C_2 = -21.805$	$C_3 = -4.9884$	$C_3 = -2.9943$

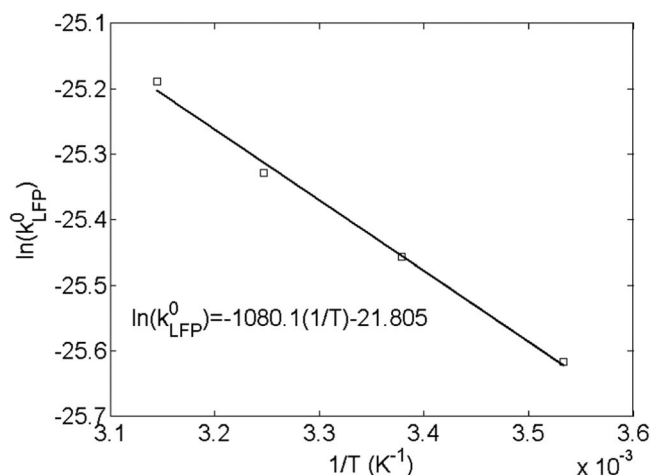


Figure 8. The logarithm of the rate constant of electrochemical reaction at the surface of LFP particles, $\ln(k_{LFP}^0)$, as a function of the inverse of temperature.

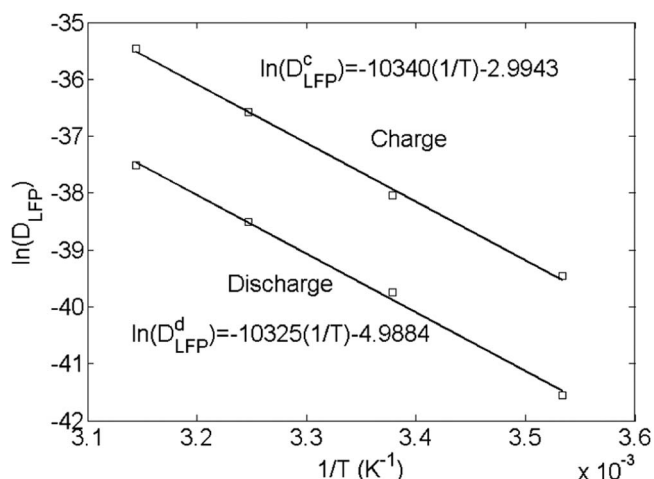


Figure 9. The logarithm of discharge-fitted, $\ln(D_{LFP}^d)$, and charge-fitted, $\ln(D_{LFP}^c)$, binary diffusion coefficient of Li^+ inside LFP particles as a function of the inverse of temperature.

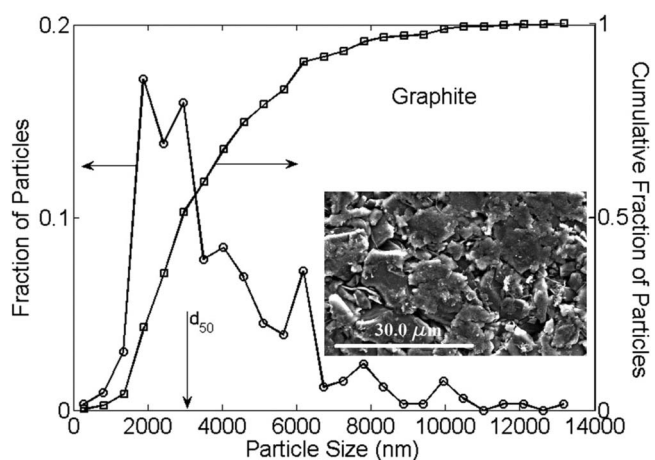


Figure 10. Particle size distribution of the graphite electrode from an analysis of the SEM image shown in the inset.

thermal water bath whose temperature varies in approximately 5°C intervals from 0°C to 23°C . However, the reported entropy change as a function of the lithium concentration in the graphite (Li_yC_6) is very small and hence is ignored here. Similar results can also be found in.^{72,87,88} Figure 11a shows the charge and discharge equilibrium potentials of the graphite where the expected multiple stages can be observed. For example, during lithium intercalation, the distinct plateau between $y \sim 0.62$ and ~ 0.9 corresponds to the formation of stage-1 graphite intercalation compound (GIC) Li_yC_6 , while the plateau between $y \sim 0.3$ and ~ 0.5 corresponds to the stage-2 GIC Li_yC_{12} formation. Another plateau between $y \sim 0.07$ and ~ 0.1 is also observed corresponding to the formation of stage-3 GIC Li_yC_{32} . Finally, at higher states of delithiation ($y < 0.07$), stage-1L graphite exists with a steep slope in equilibrium potential.^{10,43} In addition, as also seen in Figure 11a, the measured equilibrium potential for the discharge is ~ 0.02 V lower than the equilibrium potential measured for the charge. A potential hysteresis of thermodynamic origin may also exist for graphite electrodes (although, to the best of our knowledge, such a hysteresis has not been reported in the literature) which, again, cannot be explained by the model. In parallel with the LFP analysis, two equilibrium potential curves are considered separately for charge and discharge simulations as mentioned before.

Staging processes in the graphite particles are captured by the variable solid-state diffusivity model, i.e., an extremely non-ideal solid-state binary solution giving rise to a concentration-dependent thermodynamic factor. As explained in Li_yFePO_4 electrode section, the thermodynamic factor, α_G , is calculated by averaging its values

Table VII. Comparison between the scope and approach taken in this paper to fit the Li/LFP half-cell operating voltage to the scope and approach taken by Safari and Delacourt^{49,66} and Farkhondeh and Delacourt.^{24,25}

	Safari and Delacourt ^{49,66}	Farkhondeh et al. ^{24,25}	This paper
Model Differences			
Adjusted parameter to enable match of operating voltage onset and plateau	Electrochemical reaction rate constant, and four different surface resistances	Electrochemical reaction rate constant	Electrochemical reaction rate constant
Added parameters to enable match of end-of-discharge capacity variations	Different connectivity of active materials to the conductive matrix. Specifically, four different surface resistances	Expanded particle size distribution to four particle bins	Expanded particle size distribution to four particle bins
Added parameter flexibility to enable match of different charge and discharge end-capacities	Diffusion coefficient changed from constant to a function of lithium concentration	Changed the shape of the thermodynamic factor function, changing the concentration-dependence	Changed charge and discharge diffusion coefficients as per Table V
To enable matching of operating voltages at different battery temperatures	Made electrochemical reaction rate constant, and diffusion coefficient, functions of temperature	NA (Did not consider different half-cell temperatures)	Made electrochemical reaction rate constant, and diffusion coefficient, functions of temperature
Model Scope			
Maximum operating C-rate	1C Charge and discharge	1C charge 5C discharge	5C Charge and discharge
Temperatures range ($^\circ\text{C}$)	25, 45	23	10, 23, 35, 45

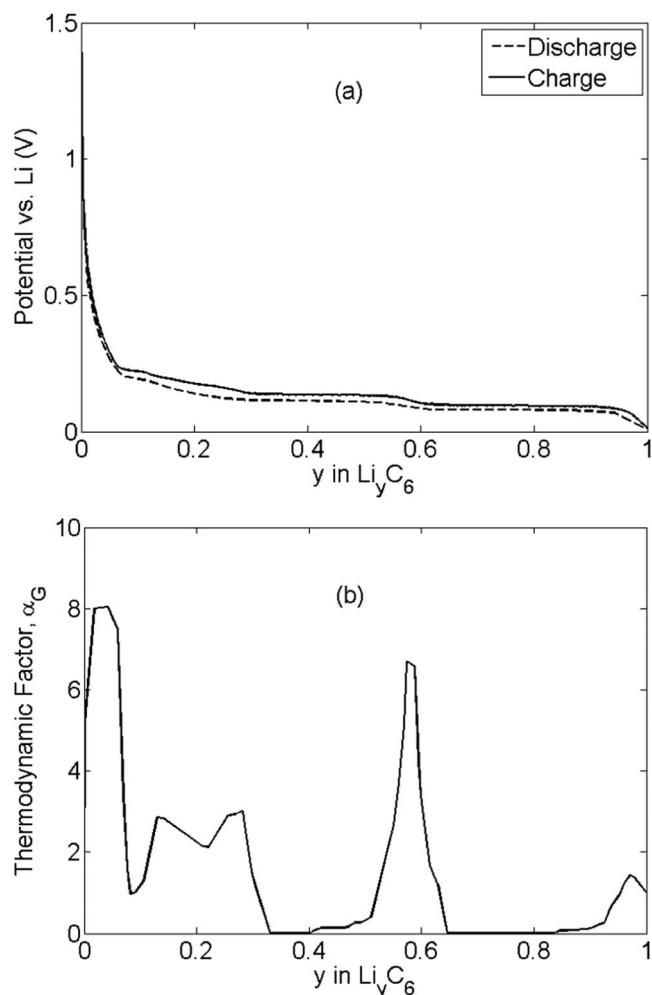


Figure 11. (a) The equilibrium potentials, and (b) the thermodynamic factor, α_G , used in discharge and charge simulations of the graphite electrode.

calculated from C/50 charge and C/50 discharge data using Equation 10.

$$\alpha_G = -\frac{F}{RT} y_G (1 - y_G) \frac{\partial U_G}{\partial y_G} \quad [10]$$

The result of this calculation is presented in Figure 11b. Several peaks are observed in Figure 11b corresponding to the aforementioned graphite stages. The low thermodynamic factor values are explained by the formation of each stage during the charging/discharging process. According to the discussion in the above paragraph, these two-phase regions, that are the plateau regions, correspond to the formation of stage-3 ($0.07 < y < 0.1$), stage-2 ($0.3 < y < 0.5$), and stage-1 ($0.62 < y < 0.9$) graphite. In these two-phase regions the thermodynamic factor is at its lowest values. As explained in Li_yFePO₄ electrode section, these low thermodynamic factors then translate to low solid-state Fickian diffusion coefficients which tend to mimic the displacement of phase-boundaries involved in an active staging process within graphite particles. Again, it should be emphasized that, although a perfectly flat voltage profile is expected during each staging step, the measured voltage values never contain perfect plateaus, thus the resulting Fickian diffusion coefficient according to the VSSD model is always greater than zero. Nonetheless, the small non-zero diffusion coefficients stem from the assumption that the binary solid-state solution is extremely non-ideal (almost immiscible), which provides an asymptotic representation of a two-phase system.

Since the electrolyte used in Li/graphite coin cell assembly is the same as that used in Li/LFP cell, the same electrolyte parameters

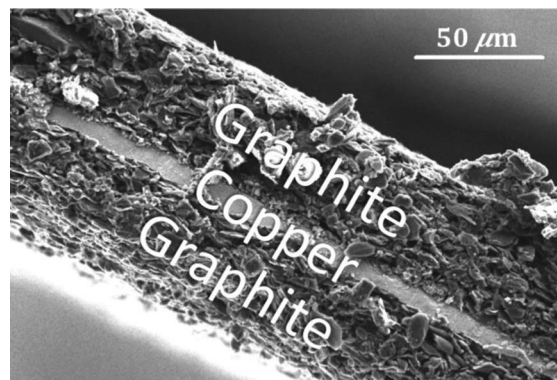


Figure 12. SEM image from cross-section of a double-sided graphite electrode.

from Li_yFePO₄ electrode section are utilized. Profilometry is utilized to measure the thickness of graphite electrode. This thickness is found to be 46 μm. As explained in Li foil kinetics temperature dependency section, an SEM image from the cross-section of the double-sided graphite electrode (shown in Figure 12) cannot be used reliably for this measurement. For comparison, the double-sided graphite electrode thickness in Figure 12 is ~96 μm while its thickness away from the electrode edges is 102 μm. Again, since the compression does not change the copper thickness, it can be measured from Figure 12 at 10 μm.

The capacity of the graphite electrode is estimated by measuring the total charge throughput at the end of a discharge process (corresponding to the cutoff potential of 0.005 V) that proceeds at the slow rate of C/50. This results in 1.242 mAh as the capacity of the graphite electrode. A 9.7 mm diameter puncher was used to cut the graphite electrode; thus the area of the electrode is known. Using the electrode area, thickness, and capacity, and utilizing the graphite theoretical capacity and density, which are 372 mAh gr⁻¹ and 2.26 gr cm⁻³,⁸⁹ respectively, the volume fraction of graphite in the electrode is determined to be ~0.432. If a typical 0.1 volume fraction is considered,⁷⁵ for the binder and other additives to the graphite electrode, the porosity of the electrode is found to be ~0.468. Since the separator used to assemble the Li/graphite coin cell is the same as the used in the Li/LFP cell assembly, all the parameters related to the separator are the same as in Li_yFePO₄ electrode section. And as in Li_yFePO₄ electrode section, the Bruggeman exponent is also 1.5 and charge transfer coefficient is set to 0.5. Finally, the maximum lithium concentration in the graphite electrodes is considered to be constant at 31,370 mol m⁻³.⁴⁹

After finding the above graphite electrode parameters, the electrochemical reaction rate constant, k_G^0 , and binary diffusion coefficient, D_G , have to be estimated. To find these parameters the simulation results of the mathematical model for the Li/graphite half-cell are fitted to the experimental galvanostatic discharge and charge data. The fitting process is first performed at 23°C and for rates ranging from C/5 to 5C. The temperature dependency of the parameters are then studied by repeating the fitting process at three more temperatures of 10°C, 35°C, and 45°C. Similar to Li_yFePO₄ electrode section, the electrochemical reaction rate constant of graphite lithiation/delithiation is evaluated by fitting the onset and plateaus of the experimental galvanostatic discharge and charge data. This value is found to be 1.5×10^{-11} mol/[m²s(mol/m³)^{1.5}] at 23°C, and is in the range reported in the literature.^{41,49,90}

Binary diffusion coefficient of the intercalated species within graphite particles is adjusted to capture the end-capacities of the experimental data. Contrary to the Li/LFP half-cell simulations, it turns out that a constant binary diffusion coefficient and only one representative particle size (d_{50}) in the graphite electrode yields satisfactory fits to all of the experimental end-capacities both on charge and on discharge. The binary diffusion coefficient of Li⁺ in graphite is obtained to be 1.0×10^{-15} m² s⁻¹ at 23°C in agreement with values reported in the literature.^{10,43,49}

Table VIII. List of the model parameters used for Li/graphite half-cell simulations at 23°C.

Parameter	Symbol	Value
Graphite charge-transfer coefficient	β_G	0.5 ^a
Li foil charge-transfer coefficient	β_{Li}	0.5 ^a
Bruggeman exponent	γ	1.5 ^a
Initial salt concentration in the electrolyte (mol m ⁻³)	c_e^0	1000 ^s
Maximum Li concentration in the graphite particles (mol m ⁻³)	c_G^{max}	31,370 ^{sa}
Graphite particle binary diffusion coefficient (m ² s ⁻¹)	\mathcal{D}_G	1.5×10^{-15} ^f
Porosity of the separator	ε_s	0.55 ^{ce}
Porosity of the graphite electrode	ε_G	0.468 ^c
Total active material volume fraction of the graphite electrode	$\varepsilon_{t,G}$	0.432 ^c
Electrochemical reaction rate constant of graphite (mol/[m ² s(mol/m ³) ^{1.5}])	k_G^0	1.5×10^{-11} ^f
Separator thickness (m)	L_s	25×10^{-6} ^{ce}
Graphite electrode thickness (m)	L_G	46×10^{-6} ^m
Effective electronic conductivity of the graphite electrode (S m ⁻¹)	σ_G^{eff}	2203.8 ^e
Li ⁺ transference number	t_+	0.38 ^v
Geometric area of the electrode (m ²)	A_G	0.739×10^{-4} ^m
Lower cutoff potential of the graphite electrode (V)	$V_{cut,G}^{min}$	0.005
Upper cutoff potential of the graphite electrode (V)	$V_{cut,G}^{max}$	1.5

(a: assumed, s: set, f: fitted, c: calculated, m: measured, sa: Safari and Delacourt,⁴⁹ ce: Celgard,⁷⁶ e: Ender et al.,⁹¹ v: Valoen and Rimeres⁷⁴).

The model parameters for the Li/graphite half-cell simulations are summarized in Table VIII. Simulation results compared to experimental galvanostatic discharge and charge data at rates ranging from C/5 to 5C and at 23°C are shown in Figure 13. Generally, good agreement between the model results and experimental data is observed in all charge and discharge rates. Figure 13a, however, illustrates that the model prediction for the half-cell end-capacity at the C/2 discharge rate is noticeably higher than the corresponding experimental value. This difference is not attributed to the number of particles used in the model as simulations using four particles did not improve the C/2 end-of-discharge deviation. This difference may be attributed to the simplicity of the mathematical model compared to the actual physics of graphite lithiation dynamics. While lithium transport inside the graphite particles includes complex mechanisms such as movement of multiple phase boundaries, grain-boundary diffusion, and diffusion in each phase, the proposed model is based on a lumped parameter, i.e., the thermodynamic factor, which may not be completely satisfactory.

Graphite properties temperature dependency.—In this section, the temperature dependency of the electrochemical reaction rate constant at the surface and the solid-state binary diffusion coefficient of Li⁺ within the graphite particles is studied. An Arrhenius relation is considered to describe these parameters as functions of temperature as follows,

$$\ln(k_G^0) = \frac{-E_{k_G^0}^a}{R} \left(\frac{1}{T} \right) + C_4 \quad [11]$$

$$\ln(\mathcal{D}_G) = \frac{-E_{\mathcal{D}_G}^a}{R} \left(\frac{1}{T} \right) + C_5 \quad [12]$$

In Equations 11 and 12, $E_{k_G^0}^a$ is the activation energy of charge-transfer reaction at the surface and $E_{\mathcal{D}_G}^a$ is the activation energy of Li⁺ diffusion within the graphite particles. C_4 and C_5 are constants with regard to the temperature. To estimate these values, a procedure similar to that explained in LiFePO₄ properties temperature dependency section is repeated here. The graphite electrochemical reaction rate constants and binary diffusion coefficients are first obtained by fitting the model to the experimental data at different temperatures of 10°C, 23°C, 35°C, and 45°C. Note that the temperature dependency of the electrolyte and lithium foil electrochemical reaction rate constants is already included in the model.

As explained in Experimental section, experiments at 10°C and 35°C were conducted at C/5 and C/2 rates, respectively whereas at 45°C the galvanostatic cycling was performed at two rates of 1C and 2C rates to assure improved accuracy. It is worth restating that according to the experimental procedure at 10°C, 35°C, and 45°C, the

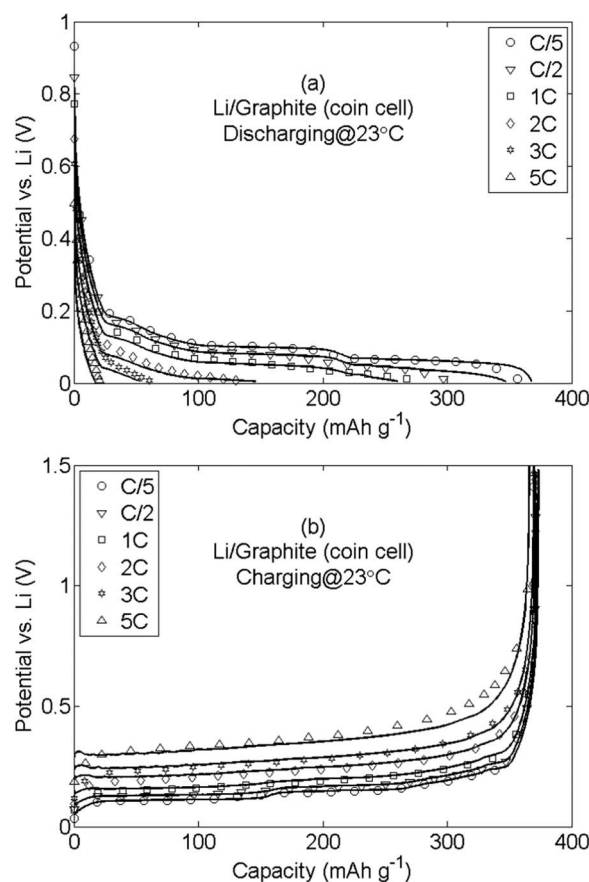


Figure 13. Comparison between the experimental data (symbols) and simulations (solid lines) of a Li/graphite half-cell for (a) galvanostatic discharge and (b) galvanostatic charge rates ranging from C/5 to 5C at 23°C.

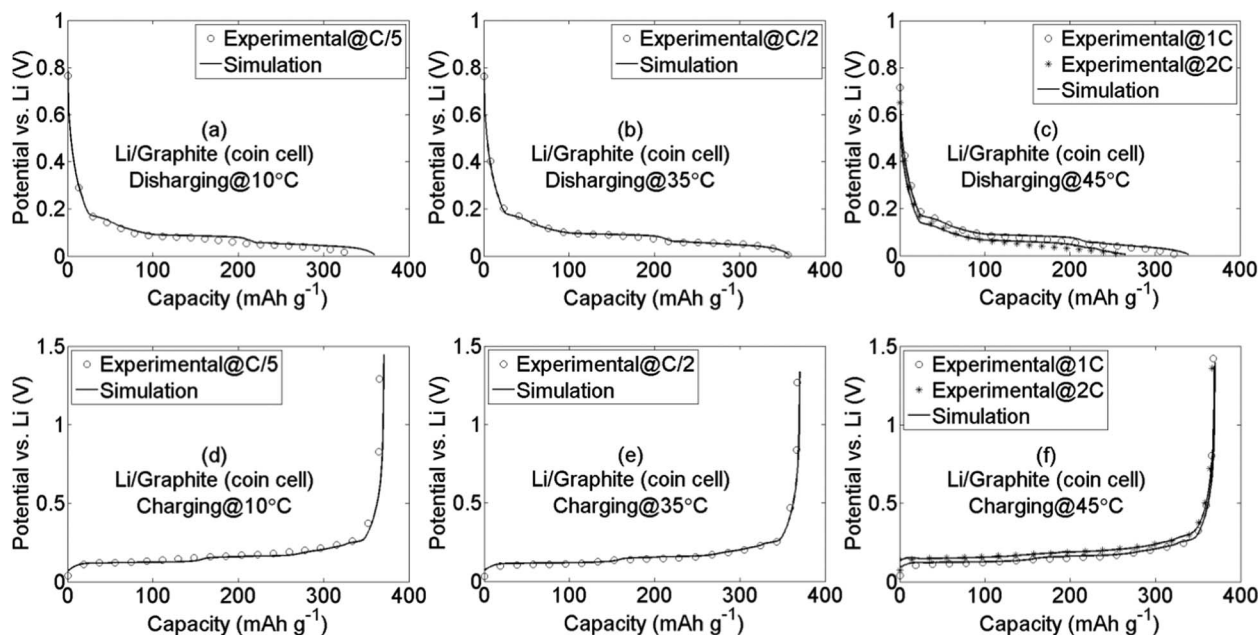


Figure 14. Fitting the experimental galvanostatic discharge and charge data with the mathematical model for (a) discharge at 10°C, (b) discharge at 35°C, (c) discharge at 45°C, (d) charge at 10°C, (e) charge at 35°C, and (f) charge at 45°C for a Li/graphite half-cell.

Table IX. The estimated kinetic and transport properties of graphite at different temperatures.

Temperature (°C)	Operating rate	Electrochemical reaction rate constant, k_{Li}^0 , (mol/[m ² s(mol/m ³) ^{1.5}])	Discharge binary diffusion coefficient, D_G , (m ² s ⁻¹)
10	C/5	1.0×10^{-11}	1.0×10^{-15}
23	C/5 to 5C	1.5×10^{-11}	1.5×10^{-15}
35	C/2	2.0×10^{-11}	2.0×10^{-15}
45	1C & 2C	2.5×10^{-11}	2.5×10^{-15}

graphite electrode was not fully charged prior to being discharged. Therefore, the initial graphite stoichiometry is adjusted to fit the initial Li/graphite half-cell operating voltage. In contrast, the graphite electrode was fully lithiated prior to being charged. The results of the fitting process at 23°C are given in Figure 13 and Table VIII. The simulation results at the other temperatures are shown in Figure 14, and the estimated electrochemical reaction rate constants and binary diffusion coefficients are listed in Table IX. The simulation results are in a good agreement with the experimental in all charge and discharge rates and temperatures.

The activation energies and constants of Equations 11 and 12 are determined by linear least square fitting Equations 11 and 12 to the estimated graphite electrochemical reaction rate constants and binary diffusion coefficients in Table IX. The resulting values are reported in Table X.

Figure 15 and Figure 16 show the curve fits used to derive the reported activation energies in Table X. It is observed that the slope of the fitted curve in Figure 16 for graphite is much smaller compared to that in Figure 9 for LFP showing diffusion in graphite is less temperature dependent compared to LFP. Therefore, an increase in the temperature of a graphite/LFP cell (e.g., the commercial cell from

which the electrodes are recovered) would improve its end-capacities mostly via an improved diffusion process in LFP. In addition, it is observed that the slope of the fitted curve in Figure 15 for graphite is higher than that in Figure 8 for LFP showing higher temperature dependency of charge-transfer kinetics at the surface of graphite particles compared to LFP particles. Note that the reported transport and kinetic parameters are valid for the discussed operating conditions and are applicable to models with similar assumptions to those adapted in

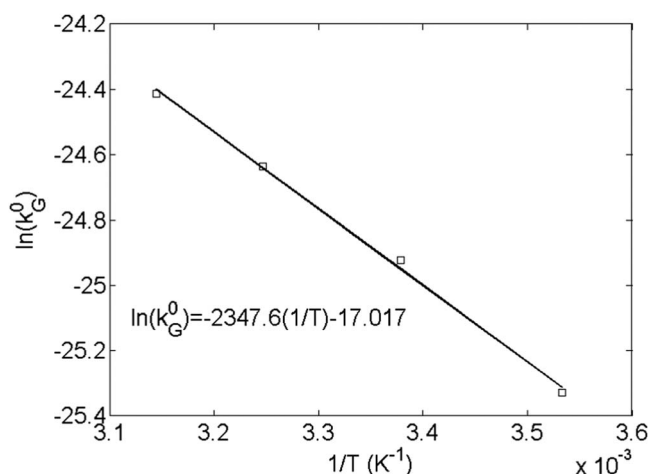


Figure 15. The logarithm of the rate constant of electrochemical reaction at the surface of graphite particles, $\ln(k_G^0)$, as a function of the inverse of temperature.

Table X. The activation energies and Equations 11 and 12 constants used to describe the temperature dependency of the kinetic and transport properties of graphite.

Parameter	Electrochemical reaction rate constant	Binary diffusion coefficient
Activation energy (J mol ⁻¹)	2×10^4	2×10^4
Constants	$C_4 = -17.017$	$C_5 = -26.227$

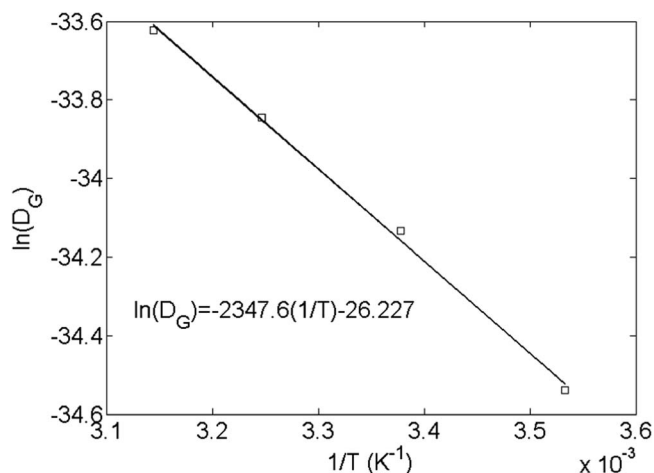


Figure 16. The logarithm of graphite binary diffusion coefficient, $\ln(D_G)$, as a function of the inverse of temperature.

this paper. However, the high quality of the fit to the data shown in this paper suggests the possibility of using the reported values at other operating conditions than those considered here.

Conclusions

An electrochemical model based on the variable solid-state diffusivity (VSSD) concept is developed and applied to Li/LFP and Li/graphite half-cells. It is shown that the model is capable of capturing the required electrode features including the rate dependency of the end-capacities on charge and discharge. This work validates simulated half-cell voltages against experimental data and extends the application of the VSSD model to a broader range of charge/discharge rates and temperatures for both LFP and graphite electrodes. It should be noted that this model is not aimed at accurately describing the phase-change process in the active material but rather targeted for engineering applications such as battery management, thermal analysis and management, and aging studies. The model is examined under constant-current condition and is yet to be assessed for other operating conditions such as potentiostatic/galvanostatic intermittent titration technique and cyclic voltammetry. Fitting simulation results to experimental voltage data at various galvanostatic charge/discharge rates (C/5 to 5C) and temperatures (10°C, 23°C, 35°C, and 45°C) provides estimates of kinetic and transport parameters for the electrode active materials over a wide range of operating conditions. As the result, the activation energies for diffusion in LFP and graphite particles are estimated to be 86 kJ mol⁻¹ and 20 kJ mol⁻¹, respectively. Furthermore, the activation energies for the charge-transfer reaction at the surface of LFP and graphite particles are 9 kJ mol⁻¹ and 20 kJ mol⁻¹, respectively. The modeling/experimental framework pursued in this paper proves more comprehensive methodology for estimating the transport and kinetic properties of graphite and LFP, and their temperature dependencies. Furthermore, this framework is general and can be applied to other battery active materials.

Acknowledgment

The authors acknowledge The Natural Sciences and Engineering Research Council of Canada (NSERC) and Transport Canada for financial support of this research project.

List of Symbols

a_k	specific surface area of the k^{th} active particle bin, m ⁻¹
C	Arrhenius equation constant
c_e	electrolyte concentration, mol m ⁻³

c_e^0	initial electrolyte concentration, mol m ⁻³
$c_{s,k}$	Li concentration inside the k^{th} active particle bin, mol m ⁻³
$c_{s,k}^0$	initial Li concentration inside the k^{th} active particle bin, mol m ⁻³
c_s^{max}	maximum Li concentration in active particles, mol m ⁻³
\bar{D}	solid-state binary diffusion coefficient, m ² s ⁻¹
D_e	electrolyte diffusion coefficient, m ² s ⁻¹
E^a	Activation energy, J mol ⁻¹
F	Faraday's constant, 96,487 C mol ⁻¹
I_{app}	current density applied to half-cells, A m ⁻²
i_k^0	exchange current density of the k^{th} active particle bin, A m ⁻²
$i_{n,k}$	reaction current density at the surface of the k^{th} active particle bin, A m ⁻²
k^0	electrochemical reaction constant, mol m ⁻² s ⁻¹ (mol m ⁻³) ^{-1.5}
L	component or half-cell thickness, m
r_k	radial distance from the center of the k^{th} active particle bin, m
R	universal gas constant, 8.314 J mol ⁻¹ K ⁻¹
$R_{p,k}$	radius of the k^{th} active particle bin, m
T	temperature, K
t	time, s
t_+^0	Li ⁺ transference number
U_k	OCP of the k^{th} active particle bin vs. Li, V
V_{cell}	operating voltage of the half-cell, V
x	distance from the Li foil/separator interface inside the cell, m
y_k	mole fraction of the Li concentration in the k^{th} active particle bin

Greek

α_k	thermodynamic factor of the k^{th} active particle bin
β	charge-transfer coefficient of the electrode
ε	component porosity
ε_k	volume fraction of the k^{th} active particle bin per unit volume of the electrode
ε_t	total volume of the cathode active material per unit volume of the electrode
η_k	surface overpotential of the k^{th} active particle bin, V
γ	Bruggeman exponent
κ	bulk ionic conductivity of the electrolyte, S m ⁻¹
κ_D	ionic diffusional conductivity of the electrolyte, A m ⁻¹
ϕ_s	electrical potential of the electrode, V
ϕ_e	electrical potential of the electrolyte, V
ϕ_{Li}	electrical potential of Li foil, V
σ	bulk electronic conductivity of electrode, S m ⁻¹

Subscripts

c	cathode
Li	Lithium foil
LFP	LiFePO ₄
s	separator
G	graphite

Superscripts

c	charge
d	discharge
eff	effective value
P	pressure

References

1. A. K. Padhi, K. S. Nanjundaswamy, and J. B. Goodenough, *Journal of Electrochemical Society*, **144**, 1188 (1997).
2. J. B. Goodenough, A. K. Padhi, K. S. Nanjundaswamy, and C. Masquelier, US Pat., 5, 910, 382, (1999).

3. S.-Y. Chung, J. T. Bloking, and Y.-M. Chiang, *Nature Materials*, **1**, 123 (2002).
4. N. Ravet, J. B. Goodenough, S. Besner, M. Simoneau, P. Hovington, and M. Armand, in: *196th Meeting of the Electrochemical Society*, Abstract # 127 Hawaii, 1999.
5. N. Ravet, Y. Chouinard, J. F. Magnan, S. Besner, M. Gauthier, and M. Armand, *Journal of Power Sources*, **97-98**, 503 (2001).
6. B. Kang and G. Ceder, *Nature*, **458**, 190 (2009).
7. A. Yamada, S. C. Chung, and K. Hinokuma, *Journal of The Electrochemical Society*, **148**, A224 (2001).
8. C. Delacourt, P. Poizot, S. Levasseur, and C. Masquelier, *Electrochemical and Solid-State Letters*, **9**, A352 (2006).
9. H. Buqa, D. Goers, M. Holzapfel, M. E. Spahr, and P. Novak, *Journal of The Electrochemical Society*, **152**, A474 (2005).
10. M. Heß and P. Novák, *Electrochimica Acta*, **106**, 149 (2013).
11. C. Wang, U. S. Kasavajjula, and P. E. Arce, *Journal of Physical Chemistry C*, **111**, 16656 (2007).
12. U. S. Kasavajjula, C. Wang, and P. E. Arce, *Journal of The Electrochemical Society*, **155**, A866 (2008).
13. S. Dargaville and T. W. Farrell, *Journal of The Electrochemical Society*, **157**, A830 (2010).
14. V. Srinivasan and J. Newman, *Journal of Electrochemical Society*, **151**, A1517 (2004).
15. Y. H. Kao, M. Tang, N. Meethong, J. Bai, W. C. Carter, and Y. M. Chiang, *Chemistry of Materials*, **22**, 5845 (2010).
16. S. Dargaville and T. W. Farrell, *Electrochimica Acta*, **94**, 143 (2013).
17. G. K. Singh, G. Ceder, and M. Z. Bazant, *Electrochimica Acta*, **53**, 7599 (2008).
18. P. Bai, D. a. Cogswell, and M. Z. Bazant, *Nano Letters*, **11**, 4890 (2011).
19. D. a. Cogswell and M. Z. Bazant, *ACS Nano*, **6**, 2215 (2012).
20. J. L. Allen, T. R. Jow, and J. Wolfenstine, *Journal of Solid State Electrochemistry*, **12**, 1031 (2007).
21. J. L. Allen, T. R. Jow, and J. Wolfenstine, *Chemistry of Materials*, **19**, 2108 (2007).
22. G. Oyama, Y. Yamada, R. Natsui, S. Nishimura, and A. Yamada, *Journal of Physical Chemistry C*, **116**, 7306 (2012).
23. I. V. Thorat, T. Joshi, K. Zaghib, J. N. Harb, and D. R. Wheeler, *Journal of The Electrochemical Society*, **158**, A1185 (2011).
24. M. Farkhondeh and C. Delacourt, *Journal of Electrochemical Society*, **159**, A177 (2012).
25. M. Farkhondeh, M. Safari, M. Pritzker, M. Fowler, T. Han, J. Wang, and C. Delacourt, *Journal of Electrochemical Society*, **161**, A201 (2014).
26. M. Mastali Majdabadi, S. Farhad, M. Farkhondeh, R. A. Fraser, and M. Fowler, *Journal of Power Sources*, **275**, 633 (2015).
27. C. Delmas, M. Maccario, L. Croguennec, F. Le Cras, and F. Weill, *Nature Materials*, **7**, 665 (2008).
28. G. Brunetti, D. Robert, P. Bayle-Guillemaud, J. L. Ouyi, E. F. Rauch, J. F. Martin, J. F. Colin, F. Bertin, and C. Cayron, *Chem. Mater.*, **23**, 4515 (2011).
29. W. C. Chueh, F. El Gabaly, J. D. Sugar, N. C. Bartelt, A. H. McDaniel, K. R. Fenton, K. R. Zavadil, T. Tylicsaczak, W. Lai, and K. F. McCarty, *Nano Letters*, **13**, 866 (2013).
30. D. Robert, T. Douillard, A. Boulineau, G. Brunetti, P. Nowakowski, D. Venet, P. Bayle-Guillemaud, and C. Cayron, *ACS Nano*, **7**, 10887 (2013).
31. M. Farkhondeh, M. Pritzker, M. Fowler, M. Safari, and C. Delacourt, *Phys. Chem. Chem. Phys.*, **16**, 22555 (2014).
32. M. Mastali, E. Samadani, S. Farhad, R. A. Fraser, and M. Fowler, in: SAE Technical Paper 2015-01-1182, 2015, Doi: 10.4271/2015-01-1182, 2015, pp. 1.
33. M. Mastali, E. Samadani, S. Farhad, R. A. Fraser, and M. Fowler, *Electrochimica Acta*, **190**, 574 (2016).
34. J. R. Dahn, *Physical Review B*, **44**, 9170 (1991).
35. N. Takami, A. Satoh, M. Hara, and T. Ohsaki, *Journal of The Electrochemical Society*, **142**, 371 (1995).
36. T. Ohzuku, *Journal of The Electrochemical Society*, **140**, 2490 (1993).
37. R. Yazami, A. Martinet, and Y. Reynier, in: I. V. Barsukov, C. S. Johnson, J. E. Doninger, and V. Z. Barsukov (Eds.), *New Carbon Based Materials for Electrochemical Energy Storage Systems*, Springer, 2006, pp. 245.
38. R. Yazami and Y. Reynier, *Journal of Power Sources*, **153**, 312 (2006).
39. M. W. Verbrugge and B. J. Koch, *Journal of The Electrochemical Society*, **150**, A374 (2003).
40. Q. Zhang, Q. Guo, and R. E. White, *Journal of The Electrochemical Society*, **153**, A301 (2006).
41. K. Kumaresan, G. Sikha, and R. E. White, *J. Electrochem. Soc.*, **155**, A164 (2008).
42. D. M. Bernardi and J.-Y. Go, *Journal of Power Sources*, **196**, 412 (2011).
43. K. G. Gallagher, D. W. Dees, A. N. Jansen, D. P. Abraham, and S.-H. Kang, *Journal of The Electrochemical Society*, **159**, A2029 (2012).
44. D. K. Karthikeyan, G. Sikha, and R. E. White, *Journal of Power Sources*, **185**, 1398 (2008).
45. D. R. Baker and M. W. Verbrugge, *Journal of Electrochemical Society*, **159**, A1341 (2012).
46. E. Tatsukawa and K. Tamura, *Electrochimica Acta*, **115**, 75 (2014).
47. M. Takahashi, S. Tobishima, K. Takei, and Y. Sakurai, *Solid State Ionics*, **148**, 283 (2002).
48. D. Y.W. Yu, C. Fietzek, W. Weydanz, K. Donoue, T. Inoue, H. Kurokawa, and S. Fujitani, *Journal of The Electrochemical Society*, **154**, A253 (2007).
49. M. Safari and C. Delacourt, *Journal of Electrochemical Society*, **158**, A562 (2011).
50. F. Jiang, P. Peng, and Y. Sun, *Journal of Power Sources*, **243**, 181 (2013).
51. T. L. Kulova, a. M. Skundin, E. a. Nizhnikovskii, and a. V. Fesenko, *Russian Journal of Electrochemistry*, **42**, 259 (2006).
52. W. Fang, O. J. Kwon, and C. Wang, *International Journal of Energy Research*, **34**, 107 (2010).
53. G. Y. Cho, J. W. Choi, J. H. Park, and S. W. Cha, *International Journal of Automotive Technology*, **15**, 795 (2014).
54. G. G. Botte, B. A. Johnson, and R. E. White, *Journal of The Electrochemical Society*, **146**, 914 (1999).
55. O. Y. Egorkina and a. M. Skundin, *Journal of Solid State Electrochemistry*, **2**, 216 (1998).
56. P. W.C. Northrop, V. Ramadesigan, S. De, and V. R. Subramanian, *Journal of The Electrochemical Society*, **158**, A1461 (2011).
57. J. Christensen, D. Cook, and P. Albertus, *Journal of The Electrochemical Society*, **160**, A2258 (2013).
58. M. Doyle, T. F. Fuller, and J. Newman, *Journal of Electrochemical Society*, **140**, 1526 (1993).
59. T. F. Fuller, M. Doyle, and J. Newman, *Journal of Electrochemical Society*, **141**, 1 (1994).
60. D. R. Baker and M. W. Verbrugge, *Journal of The Electrochemical Society*, **159**, A1341 (2012).
61. J. Newman and K. E. Thomas-Alyea, *Electrochemical Systems*, 3rd ed., Wiley-IEEE, 2004.
62. COMSOL Multiphysics, User's Guide, Version 4.4, COMSOL Inc., 2015.
63. MATLAB, Curve Fitting Toolbox™ User's Guide, 2015.
64. K. E. Thomas and J. Newman, *J. Electrochem. Soc.*, **150**, A176 (2003).
65. I. V. Thorat, *Understanding Performance-Limiting Mechanisms in Li-Ion Batteries for High-Rate Applications*, Brigham Young University, 2009.
66. M. Safari and C. Delacourt, *Journal of Electrochemical Society*, **158**, A63 (2011).
67. M. Guo, G. Sikha, and R. E. White, *Journal of Electrochemical Society*, **158**, A122 (2011).
68. W. Dreyer, J. Jamnik, C. Guhlke, R. Huth, J. Moskon, and M. Gaberscek, *Nature Materials*, **9**, 448 (2010).
69. J. L. Dodd, Phase Composition and Dynamical Studies of Lithium Iron Phosphate, California Institute of Technology, 2007.
70. J. L. Dodd, S. Nishimura, R. Yazami, A. Yamada, and B. Fultz, *210th ECS Meeting*, Abstract #179 (2006).
71. A. Yamada, H. Koizumi, S.-I. Nishimura, N. Sonoyama, R. Kanno, M. Yonemura, T. Nakamura, and Y. Kobayashi, *Nature Materials*, **5**, 357 (2006).
72. K. Jalkanen, T. Aho, and K. Vuorilehto, *Journal of Power Sources*, **243**, 354 (2013).
73. M. Safari, M. Farkhondeh, M. Pritzker, M. Fowler, T. Han, and S. Chen, *Electrochimica Acta*, **115**, 352 (2014).
74. L. O. Valøen and J. N. Reimers, *Journal of The Electrochemical Society*, **152**, A882 (2005).
75. Y. Li, S. Meyer, J. Lim, S. C. Lee, W. E. Gent, S. Marchesini, H. Krishnan, T. Tylicsaczak, D. Shapiro, A. L.D. Kilcoyne, and W. C. Chueh, *Advanced Materials*, **27**, 6591 (2015).
76. LLC Celgard, CELGARD 2500 Product Information (2015).
77. M. Doyle, J. Newman, A. S. Gozdz, C. N. Schmulz, and J.-M. Tarascon, *Journal of Electrochemical Society*, **143**, 1890 (1996).
78. E. Prada, D. Di Domenico, Y. Creff, J. Bernard, V. Sauvant-Moynot, and F. Huet, *Journal of The Electrochemical Society*, **159**, A1508 (2012).
79. V. Srinivasan and J. Newman, *Electrochemical and Solid-State Letters*, **9**, A110 (2006).
80. D. Morgan, A. Van der Ven, and G. Ceder, *Electrochemical and Solid-State Letters*, **7**, A30 (2004).
81. H. C. Shin, K. Y. Chung, W. S. Min, D. J. Byun, H. Jang, and B. W. Cho, *Electrochemistry Communications*, **10**, 536 (2008).
82. A. V. Churikov, A. V. Ivanishchev, I. A. Ivanishcheva, V. O. Sycheva, N. R. Khasanova, and E. V. Antipov, *Electrochimica Acta*, **55**, 2939 (2010).
83. H. Matsui, T. Nakamura, Y. Kobayashi, M. Tabuchi, and Y. Yamada, *Journal of Power Sources*, **195**, 6879 (2010).
84. P. Bai and M. Z. Bazant, *Nature Communications*, **5**, 3585 (2014).
85. Y. Reynier, R. Yazami, and B. Fultz, *Journal of Power Sources*, **119-121**, 850 (2003).
86. Y. F. Reynier, R. Yazami, and B. Fultz, *Journal of The Electrochemical Society*, **151**, A422 (2004).
87. K. E. Thomas and J. Newman, *Journal of Power Sources*, **119-121**, 844 (2003).
88. R. E. Williford, V. V. Viswanathan, and J.-G. Zhang, *Journal of Power Sources*, **189**, 101 (2009).
89. M. Alias, O. Crosnier, I. Sandu, G. Jestin, A. Papadimitopoulos, F. Le Cras, D. M. Schleich, and T. Brousse, *Journal of Power Sources*, **174**, 900 (2007).
90. V. R. Subramanian, V. Boovaragavan, V. Ramadesigan, and M. Arabandi, *Journal of Electrochemical Society*, **156**, A260 (2009).
91. M. Ender, A. Weber, and E. Ivers-Tiffée, *Electrochemistry Communications*, **34**, 130 (2013).